

1 Revision 01

2 Word Count: 6793

3 Oxygen isotope ratios in zircon and garnet: A record of assimilation and fractional crystallization  
4 in the Dinkey Dome peraluminous granite, Sierra Nevada, CA

5

6 Raiza R. Quintero<sup>1\*</sup>, Kouki Kitajima<sup>1</sup>, Jade Star Lackey<sup>2</sup>, Reinhard Kozdon<sup>1,3</sup>, Ariel Strickland<sup>1</sup>,  
7 and John W. Valley<sup>1</sup>

8

9 <sup>1</sup>WiscSIMS, Department of Geoscience, University of Wisconsin, Madison, WI, 53706, USA

10 <sup>2</sup> Geology Department, Pomona College Claremont, CA, 91711, USA

11 <sup>3</sup> Lamont-Doherty Earth Observatory of Columbia University, Palisades, NY, 10964, USA

12

13 For submission to *American Mineralogist* (John Valley Issue)

14

15

16

17

18

19

20 \*Corresponding Author present address:

21 Space Science Technology Centre, School of Earth and Planetary Science, Curtin University of

22 Technology GPO Box U1987, Perth, WA, 6845 Australia

23 [r.quinteromendez@postgrad.curtin.edu.au](mailto:r.quinteromendez@postgrad.curtin.edu.au)

24 **Abstract**

25 The 119 Ma Dinkey Dome pluton in the central Sierra Nevada Batholith is a  
26 peraluminous granite and contains magmatic garnet and zircon that are complexly zoned with  
27 respect to oxygen isotope ratios. Intracrystalline SIMS analysis tests the relative importance of  
28 magmatic differentiation processes vs. partial melting of metasedimentary rocks. Whereas  $\delta^{18}\text{O}$   
29 values of bulk zircon concentrates are uniform across the entire pluton (7.7‰ VSMOW), zircon  
30 crystals are zoned in  $\delta^{18}\text{O}$  by up to 1.8‰, and when compared to late garnet, show evidence of  
31 changing magma chemistry during multiple interactions of the magma with wall rock during  
32 crustal transit. The evolution from an early high- $\delta^{18}\text{O}$  magma [ $\delta^{18}\text{O}(\text{WR}) = 9.8\%$ ] towards lower  
33 values is shown by high  $\delta^{18}\text{O}$  zircon cores (7.8‰) and lower  $\delta^{18}\text{O}$  rims (6.8‰). Garnets from the  
34 northwest side of the pluton show a final increase in  $\delta^{18}\text{O}$  with rims reaching 8.1‰. In situ REE  
35 measurements show zircon is magmatic and grew before garnets. Additionally,  $\delta^{18}\text{O}$  in garnets  
36 from the western side of the pluton are consistently higher (Ave = 7.3‰) relative to the west  
37 (Ave = 5.9‰).

38 These  $\delta^{18}\text{O}$  variations in zircon and garnet record different stages of assimilation and  
39 fractional crystallization whereby an initially high  $\delta^{18}\text{O}$  magma partially melted low  $\delta^{18}\text{O}$   
40 wallrock and was subsequently contaminated near the current level of emplacement by higher  
41  $\delta^{18}\text{O}$  melts. Collectively, the comparison of  $\delta^{18}\text{O}$  zoning in garnet and zircon shows how a  
42 peraluminous pluton can be constructed from multiple batches of variably contaminated melts,  
43 especially in early stages of arc magmatism where magmas encounter significant heterogeneity  
44 of wall-rock assemblages. Collectively, peraluminous magmas in the Sierran arc are limited to  
45 small < 100 km<sup>2</sup> plutons that are intimately associated with metasedimentary wallrocks and often  
46 surrounded by later and larger, metaluminous tonalite and granodiorite plutons. The general

47 associations suggest that early stage arc magmas sample crustal heterogeneities in small melt  
48 batches, but that with progressive invigoration of the arc, such compositions are more effectively  
49 blended with mantle melts in source regions. Thus, peraluminous magmas provide important  
50 details of the nascent Sierran arc and pre-batholithic crustal structure.

51 **Keywords:** peraluminous granite, garnet, zircon, Sierra Nevada, oxygen isotopes, REE, SIMS

## 52 **Introduction**

53 The petrogenesis of peraluminous granites is a longstanding question (Clemens and Wall  
54 1981; Patiño Douce and Johnston 1991; Frost et al. 2001; Villaros et al. 2009; Lackey et al.  
55 2011). Peraluminous composition in granitoid rocks is defined by molar proportions of  $\text{Al}_2\text{O}_3$  in  
56 excess of combined  $\text{CaO}$ ,  $\text{Na}_2\text{O}$ , and  $\text{K}_2\text{O}$ :  $\text{Al}_2\text{O}_3/(\text{CaO}+\text{K}_2\text{O}+\text{Na}_2\text{O}) > 1$ , or an aluminum  
57 saturation index ( $\text{ASI} > 1$ ; Zen 1988). Peraluminous granitoids typically form from a high  
58 proportion of melts of aluminous crustal or sedimentary source rocks (Chappell and White 1974;  
59 Scaillet et al. 2016). Alternative mechanisms can explain the generation of weakly peraluminous  
60 compositions in granitoid rocks (e.g. fractional crystallization, crustal anatexis and vapor phase  
61 transfer; Zen 1988).

62 Isotope tracers can discriminate between source, magmatic differentiation, and  
63 contamination characteristics of peraluminous magmas. Early work showed correlated  $^{87}\text{Sr}/^{86}\text{Sr}$   
64 and  $\delta^{18}\text{O}$  as indicative of crustal melting (O'Neil and Chappell 1977; Halliday et al. 1981).  
65 Oxygen isotope ratios are affected by assimilation of crustal rocks, which have different  $\delta^{18}\text{O}$   
66 values than mantle-derived magmas (e.g., Taylor and Sheppard 1986; Valley et al. 2005). In  
67 cases where crustal melts are produced from young source rocks, radiogenic isotopes are not  
68 sensitive, and oxygen isotopes are typically the most sensitive isotopic tracer (e.g., Valley 2003;  
69 Lackey et al. 2011; Jeon et al. 2012).

70 Oxygen isotopes can be measured in retentive zoned minerals to record information about  
71 magma evolution (e.g., Valley 2003; Bindeman 2008; Lackey et al. 2011). Self-diffusion rates of  
72 oxygen in garnet and zircon are among the slowest in common minerals (Coughlan 1990; Wright  
73 et al. 1995; Watson and Cherniak 1997; Vielzeuf et al. 2005; Page et al. 2007a, 2010; Bowman  
74 et al. 2011), and crystallization of both minerals in peraluminous granites allows them to be used  
75 in tandem to record a more complete time history than would be provided by a single mineral  
76 (Lackey et al. 2011). The  $\delta^{18}\text{O}$  values of zircon and garnet are quenched upon crystallization and  
77 growth zoning provides a record of magmatic evolution (King and Valley 2001; Valley 2003;  
78 Lackey et al. 2006).

79 Zircon and other accessory minerals also record the rare earth element (REE)  
80 compositions of felsic magmas during their growth (Sawka and Chappell 1988; Hoskin et al.  
81 2000; Hoskin and Schaltegger 2003). Rare earths are incorporated in zircon by coupled  
82 substitution mechanisms (Speer 1982; Hinton and Upton 1991; Halden et al. 1993; Hoskin and  
83 Ireland 2000; Finch et al. 2001; Hoskin and Schaltegger 2003).

84 In this study, we employ secondary ion mass spectrometry (SIMS) to measure oxygen  
85 isotope ratios ( $\delta^{18}\text{O}$ ) and trace element compositions, including Y + REEs. The SIMS method  
86 provided accurate and precise measurements of intracrystalline zoning at high spatial resolution  
87 (ca. 10  $\mu\text{m}$ ) in zircon and garnet crystals collected throughout the Dinkey Dome granite (Fig. 1).  
88 The zoning measured within these crystals is useful to contextualize contamination, assimilation,  
89 and/or high temperature alteration processes during growth of both zircon and garnet.

90 The resulting data constrain models for the origin and contamination of silicic melts in  
91 the Sierra Nevada batholith. The processes that formed this and other granites *senso stricto* in the  
92 Sierra are critical to understand the relative contribution of preexisting crust in the Sierran arc

93 and evaluate the different processes that affected the composition of final magmas. Thus, in situ  
94 analysis of refractory magmatic minerals helps in discriminating the relative amounts of crustal  
95 contribution by: crystal fractionation and partial melting of mafic magmas, where no crustal  
96 contribution is required in the production of felsic magmas (Ratajeski et al. 2001, 2005; Wenner  
97 and Coleman 2004); contamination, assimilation and fractional crystallization whereby magmas  
98 become silicic (Lackey et al., 2005, 2006, 2008; Nelson et al. 2013); and wholesale melting of  
99 crustal material by deep heat sources with no contribution of mafic material (Holden et al. 1987).

## 100 **Geology**

### 101 **The Sierra Nevada Batholith**

102 The voluminous Cretaceous Sierra Nevada batholith, California (Fig. 1) consists mainly  
103 of tonalite to granodiorite plutons to depths of ~35 km (Saleeby et al. 2003), with more mafic  
104 diorite and refractory gabbroic residues continuing to ca. 45 km (Fliedner et al. 2000). Gabbro  
105 complexes and mafic enclaves are a common but volumetrically small part of the batholith and  
106 have been targeted to study the mass balance of mantle and crustal melt inputs to produce the  
107 intermediate, granodiorite compositions that are the bulk of the batholith (Dorais et al. 1990;  
108 Coleman et al. 2004; Wenner and Coleman 2004). Other studies have examined the sub-arc  
109 mantle and residual mafic root of the batholith, sampled as pyroxenite, garnet-clinopyroxenite,  
110 and lherzolite xenoliths in Cenozoic volcanic rocks (Moore and Dodge 1980; Ducea 2001; Lee et  
111 al. 2006; Chin et al. 2014). Such studies provide additional information on mantle controls of  
112 magmatic heat budgets and mafic magma flux, revealing in detail that multi-stage crystallization  
113 and re-melting episodes are required to build granodioritic crust that complements the major  
114 element (e.g., Mg) and isotopic compositions of xenoliths. In addition, experimental studies

115 show that high silica melts can be produced from re-melting of Sierran gabbros (Sisson et al.  
116 2005; Ratajeski et al. 2005)

117         Despite considerable attention to magmatic origins recorded in mafic to ultramafic rocks,  
118 few studies have focused on potential high-silica melts;  $\delta^{18}\text{O}$  studies of granodiorite and tonalite  
119 suites require at least 15-30% input of melts from supracrustal sources, thus partial melting of  
120 gabbros is not the sole source of potential high-silica end-member melts. Thus, direct studies of  
121 rocks with relatively undiluted high-silica crustal melts are important, but only a handful have  
122 been undertaken: Wenner and Coleman (2004) studied several granites in a regional survey of  
123 both mafic and felsic plutons in the Sierra; Zeng et al. (2005) examined partial melting in a lower  
124 crustal migmatite complex in the Southern Sierra Nevada; Lackey et al. (2006) studied regional  
125 and pluton-scale patterns of  $\delta^{18}\text{O}$  of peraluminous granites in the Sierra. These three studies  
126 found evidence of crustal melting in the granitic plutons and migmatites, highlighting the  
127 importance of such melts as a factor in the isotopic variability in many Sierran granodiorites,  
128 hence, added motivation to study the Dinkey Dome granite.

### 129 **The Dinkey Dome granite**

130         The garnet, two-mica Dinkey Dome granite is a relatively small ( $\sim 30 \text{ km}^2$ ) pluton  
131 surrounded by granodiorite plutons (e.g., Dinkey Creek Granodiorite) and other granites of the  
132 Shaver Intrusive Suite (Figs. 1 and 2; Bateman 1992; Lackey et al. 2006). With a U-Pb zircon  
133 age of 119 Ma (Frazer et al. 2008), the Dinkey Dome pluton is coeval with the oldest members  
134 of the Fine Gold Intrusive Suite to the west, and significantly older than other members of the  
135 Shaver Intrusive Suite (Frazer et al. 2008). Thus, the Dinkey Dome represents a case of  
136 magmatism that was anomalously inboard of the broad magmatic “locus” in the Sierra at the  
137 time it was emplaced, and a departure from the broad trend of eastward-younging Cretaceous

138 intrusive suites in the Sierran Arc (Chen and Moore 1982; Memeti et al. 2010; Davis et al. 2012;  
139 Lackey et al. 2012; Ardill et al. 2018; Chapman and Ducea 2019). Initial  $^{87}\text{Sr}/^{86}\text{Sr}$  ratios of the  
140 Dinkey Dome granite are 0.7065 (Kistler and Peterman 1973). Metamorphic wallrocks consist of  
141 quartzite, mica schist, biotite hornfels, and marble (Fig. 2) (Bateman and Wones 1972). The  
142 chemistry of the pluton and aluminous minerals (garnet, muscovite,  $\text{Al}_2\text{SiO}_5$ ) contained therein  
143 are typical for peraluminous granites. Whole rock geochemical analyses of the Dinkey Dome  
144 show that aluminum saturation indices (ASI) are peraluminous (west side ASI = 1.02; east side  
145 ASI = 1.07; Lackey et al. 2006). Average garnet compositions in the Dinkey Dome granite are  
146  $\text{Alm}_{72.4}\text{Sps}_{19.5}\text{Pyp}_{5.8}\text{Grs}_{2.3}$  on the west and  $\text{Alm}_{78.6}\text{Sps}_{19.1}\text{Pyp}_{0.9}\text{Grs}_{1.4}$  on the east. There are no  
147 garnet-bearing metamorphic wallrocks in contact with the Dinkey Dome, consistent with the  
148 magmatic origin of garnet (Lackey et al. 2011). Shallow crystallization is inferred by scattered  
149 miarolitic cavities in the east side of the pluton that are inferred to indicate a pressure of <1 kbar  
150 (Wones et al. 1969). The preservation of coarse, euhedral books of muscovite, suggests some of  
151 the muscovite formed at depth, and was preserved during ascent and final crystallization of the  
152 magma. The Dinkey Creek Granodiorite, which is ~8 million years younger than the Dinkey  
153 Dome granite (Frazer et al. 2008), engulfs the Dinkey Dome pluton and its pendant. Al-in-  
154 hornblende pressure estimates of the Dinkey Creek Granodiorite are  $4.0 \pm 0.4$  kbar, from 10  
155 widely distributed samples collected by Ague and Brimhall (1988a) and recalculated by Tobisch  
156 et al. (1993). The pressures derived from hornblende in the Dinkey Creek Granodiorite imply  
157 considerable difference of depth, although, hornblende may just record early, deeper magmatic  
158 conditions which is plausible given increasing evidence of hornblende populations showing a  
159 continuum of magma conditions (Barnes et al. 2017). Nevertheless, the pressure/age differential  
160 implies 10 km of burial of the Dinkey Dome granite and its pendant rocks in 8 million years.

161 Construction of younger batholith rocks with higher apparent pressures around pendants  
162 and older plutons that are relatively shallow is seen elsewhere in the Sierra Nevada. For instance,  
163 recent oxygen isotope analysis of skarn garnets in the Mineral King pendant (85 km SE) shows  
164 paleo-hydrothermal systems were infiltrated by meteoric water at ca. 135 Ma (Ryan-Davis et al.  
165 2019) and again at ca. 109 Ma (D'Errico et al. 2012), but that younger (98 Ma) voluminous  
166 granodiorite plutons surround the pendant and these hydrothermal systems record apparent  
167 emplacement pressures of ca. 3 kbar (Ague and Brimhall 1988b), deeper than the possible brittle-  
168 ductile transition that would permit extensive meteoric water circulation. Similarly, volcanic  
169 rocks in the Ritter Range pendant (60 km N) have steep, down-dip stretching lineations and are  
170 found adjacent to slightly younger plutonic rocks (Tobisch et al. 2000). This juxtaposition of  
171 younger shallow plutons against older, higher pressure rocks, suggests that the older rocks were  
172 engulfed by later magmas as the batholith is built around them through interplays of bulk-arc  
173 thickening, structural shortening, or a density driven settling (e.g., Glazner and Miller, 1997).

174 **Petrography.** The Dinkey Dome granite contains quartz, plagioclase, K-feldspar, zircon,  
175 biotite and muscovite, and commonly has garnet, perthite, sericitized feldspar, granophyre and  
176 myrmekite. Accessory phases include zircon, monazite, apatite, magnetite and ilmenite.  
177 Andalusite and sillimanite show scattered occurrence on the eastern side of the pluton (Guy,  
178 1980). Molybdenite and uraninite have been reported on the eastern side as well (Lackey et al.,  
179 2006). Andalusite has textural traits indicative of magmatic crystallization, including uniformly  
180 sized and distributed, euhedral to subhedral grains free of carbonaceous chiastolite inclusions  
181 that are typically associated with metamorphic andalusite (Clarke et al. 2005). Where observed,  
182 fibrolitic sillimanite is uniformly distributed in the granite and does not appear to form at the  
183 expense of andalusite or vice versa. The concentration of fibrolite toward the interior of the



184 pluton was interpreted to record high temperatures in the interior of that domain that may have  
185 lasted longer. Guy (1980) also noted fine-grained, secondary muscovite replacing andalusite and  
186 sillimanite, likely forming under subsolidus conditions (Guy, 1980), unlike early, phenocrystic  
187 muscovite; thus, muscovite and aluminosilicates in the pluton likely integrate varying P-T  
188 conditions as magma ascended, was contaminated, and crystallized. Analyses of  $\delta^{18}\text{O}$  (And) in  
189 two samples showed values consistent with magmatic crystallization; values of 8.5‰ are ~2‰  
190 lower than pluton  $\delta^{18}\text{O}$  (WR) values whereas adjacent wallrock  $\delta^{18}\text{O}$  values are 3-4‰ higher  
191 than andalusite and inconsistent with high temperature equilibrium. Values of  $\delta^{18}\text{O}$  of fibrolite  
192 from one sample are similar to co-existing andalusite, a result consistent with crystallization of  
193 the two minerals from the same magma (Lackey et al. 2006).

194 **Garnet and Zircon: occurrence, morphology and internal structures.** Magmatic  
195 garnet occurs throughout the Dinkey Dome and is found in all the samples collected in this study  
196 and by Lackey et al. (2006). Unlike other peraluminous plutons in the Sierra Nevada where  
197 garnet is concentrated near contacts, magmatic garnet in the Dinkey Dome occurs throughout the  
198 entire pluton. These crystals are generally subhedral to euhedral and range in size from 200-2000  
199  $\mu\text{m}$ . The pluton contains both pink and red garnet. Garnet in the west side of the pluton is darker  
200 (red) vs. lighter (pink) in the east side. BSE imaging reveals subtle concentric oscillatory growth-  
201 zoning within these grains. Garnet grains aren't generally inclusion-rich and the distribution of  
202 inclusions from grain-to-grain is not uniform throughout the samples. Garnet crystals contain  
203 inclusions of plagioclase, K-feldspar, muscovite, biotite, quartz, monazite, apatite, ilmenite and  
204 zircon (Fig. 3).

205 Zircon in the Dinkey Dome granite occurs as euhedral crystals that range in size from 20  
206 to 300  $\mu\text{m}$  but are generally ~100  $\mu\text{m}$  long and 25-50  $\mu\text{m}$  wide. In some cases, zircon crystals

207 occur as inclusions within garnet (Figs. 3c and d). Conversely, some zircon grains contain  
208 inclusions of quartz, K-feldspar, apatite, plagioclase, biotite, ilmenite, and magnetite that have  
209 been identified by EDS. Ortiz (2010) examined 50 zircons by SEM in a polished grain mount  
210 from sample 1S79 and found apatite inclusions in 9 zircon grains, K-feldspar in 8, quartz in 4,  
211 biotite in 2, and Fe-Ti oxide in 1. BSE and CL imaging reveals oscillatory zoning; convolute  
212 zoning is present in some zircon cores. Representative textures are seen in Figure 4.

### 213 **Previous isotopic work**

214 Lackey et al. (2006) analyzed  $\delta^{18}\text{O}$  by laser fluorination of garnet (Grt), zircon (Zrn),  
215 quartz (Qz), andalusite (And) and whole rock powders (WR) in the Dinkey Dome pluton (Fig. 2)  
216 as part of a regional study of peraluminous granitoid plutons in the Sierra Nevada. Their study  
217 produced several key results. First, values of  $\delta^{18}\text{O}$  are elevated:  $\delta^{18}\text{O}(\text{WR}) = 9.6\text{--}10.4\text{‰}$   
218 VSMOW,  $\delta^{18}\text{O}(\text{Qz}) = 10.6\text{--}11.3\text{‰}$ ,  $\delta^{18}\text{O}(\text{And}) = 8.4\text{--}8.5\text{‰}$ ,  $\delta^{18}\text{O}(\text{Zrn}) = 7.0\text{--}7.8\text{‰}$ , and  
219  $\delta^{18}\text{O}(\text{Grt}) = 6.7\text{--}7.4\text{‰}$ . The surrounding Kings Sequence metasedimentary rocks (marbles,  
220 hornfels, and quartzites) of the Dinkey Creek pendant have  $\delta^{18}\text{O}(\text{WR})$  of  $9.5\text{--}11.6\text{‰}$ . Other  
221 peraluminous granites in the Sierra Nevada Batholith also have high  $\delta^{18}\text{O}(\text{Zrn}) > 7.5\text{‰}$ , while  
222 metaluminous granitic rocks near the Dinkey Dome have average zircon  $\delta^{18}\text{O}$  values that range  
223 from  $6.5\text{--}7.5\text{‰}$  (Lackey et al. 2006, 2008).

224 Values of  $\delta^{18}\text{O}$  for zircon, quartz and whole rock are unimodal across the entire pluton,  
225 however,  $\delta^{18}\text{O}$  values of magmatic garnet are bimodal, decreasing by  $\sim 0.6\text{‰}$  on the east side of  
226 the central metasedimentary septum within the Dinkey Dome (Fig. 2). High  $\delta^{18}\text{O}$  values and  
227 equilibrium fractionations of garnet and zircon on the west side of the pluton ( $\Delta^{18}\text{O}(\text{Grt-Zrn}) =$   
228  $0.06 \pm 0.13\text{‰}$ ), indicate that prior to the crystallization of both minerals, the magma was elevated  
229 in  $\delta^{18}\text{O}$ . On the eastern side,  $\delta^{18}\text{O}$  values of garnet are lower and not equilibrated with zircon

230 ( $\Delta^{18}\text{O}(\text{Grt-Zrn}) = -0.6 \pm 0.13\text{‰}$ ), recording a change in magmatic  $\delta^{18}\text{O}$  synchronous with  
231 crystallization. These differences in fractionation are small but distinct. The lower  $\delta^{18}\text{O}$  values in  
232 garnet that formed later than zircons, seen as inclusions in garnet (Figs. 3c and d), suggest that  
233 low  $\delta^{18}\text{O}$  material was assimilated after the crystallization of zircon and before crystallization of  
234 garnet. These results are interpreted to indicate that the Dinkey Dome granitic magmas evolved  
235 through contamination by low  $\delta^{18}\text{O}$  material, however no low  $\delta^{18}\text{O}$  country rocks are exposed in  
236 the Dinkey Creek Pendant. Thus, partial melting of such a low  $\delta^{18}\text{O}$  contaminant would be  
237 required to have occurred deeper in the crust (Lackey et al. 2006).

## 238 **Methods**

### 239 **Sample preparation and imaging**

240 Zircon and garnet mineral separates of ten samples from Lackey et al. (2006) (samples  
241 1S51 to 1S82) were handpicked and cast in 25-mm diameter round epoxy mounts along with the  
242 Kim-5 zircon (Valley 2003) and UWG-2 garnet (Valley et al. 1995) standards, ground to the  
243 level of best mineral exposure, polished to a smooth, flat, low-relief surface, and carbon coated  
244 prior to imaging. Secondary Electron (SE), Backscattered Electron (BSE) and  
245 Cathodoluminescence (CL) images were obtained for each grain, and Energy Dispersive X-ray  
246 Spectrometry (EDS) was conducted using the UW-Madison, Dept. of Geoscience Hitachi S-  
247 3400N SEM (Scanning Electron Microscope). Based on the images obtained, approximately 10  
248 zircon grains (that display distinctive rims and cores) and five garnet grains were chosen for in  
249 situ analysis from each sample. The SEM images were also used to locate the positions for SIMS  
250 analyses. Carbon coats were then removed, and the mounts were coated with gold for SIMS  
251 analysis.

252 Twenty-five-mm round thin sections were made of samples collected during this study  
253 (samples 10DD02-10DD19, Table 1, Supplementary Table A) (Fig. 2) and top mounted with  
254 UWQ-1 quartz standard (Kelly et al. 2007) and UWG-2 in their centers. Isotopic analysis of  
255 minerals in thin section rather than in grain mounts permits detailed descriptions of zircon and  
256 garnet that are in known petrographic relation to each other. Imaging prior to SIMS analysis was  
257 conducted in the same manner as described above.

### 258 **Major and minor element analyses of garnet by electron microprobe**

259 Determination of composition and testing for compositional zoning preceded every SIMS  
260  $\delta^{18}\text{O}$  analysis of garnet. Major and minor element analyses of garnet were obtained using the  
261 UW-Madison, Dept. of Geoscience CAMECA SX51 electron microprobe by wavelength  
262 dispersive spectrometry. Eight elements were analyzed: Si, Al, Fe, Mg, Mn, Ca, Ti, and Cr  
263 (Supplementary Table B). The operating conditions were accelerating potential of 15KeV, 40°  
264 takeoff angle, and a fixed focused beam at 20 nA. Counting time for all elements was 10 seconds  
265 on-peak and 10 seconds off-peak. LIF, PET, and TAP analyzer crystals were used to acquire  $K\alpha$   
266 X-ray intensities for Mn, Fe and Cr; Ca and Ti; and Al, Si and Mg, respectively. Crystalline  
267 standards were used: Minas Gerais rutile for Ti; U.W. synthetic fayalite for Fe; synthetic  
268 tephroite for Mn; USNM 143968 Kakanui pyrope for Mg; Andradite<sub>99</sub>-Rota (Hungary) for Ca;  
269 synthetic  $\text{Cr}_2\text{O}_3$  for Cr; and HU Almandine<sub>56</sub> for Al and Si.

### 270 **Laser Fluorination analysis of $\delta^{18}\text{O}$**

271 In order to assess any correlation of chemical composition with  $\delta^{18}\text{O}$ , individual garnet  
272 grains (~1.5-2.0 mg) from 10 samples previously studied by Lackey et al. (2006) were analyzed  
273 in the UW-Madison, Dept. of Geoscience Stable Isotope Laboratory by laser fluorination using  
274  $\text{BrF}_5$  as the reagent. A dual-inlet gas-source Finnigan/MAT 251 mass spectrometer was used to

275 measure isotope ratios. Standardization was done using UWG-2 ( $\delta^{18}\text{O} = 5.80 \text{ ‰ VSMOW}$ ),  
276 which provides high precision and accuracy in laser analyses (Valley et al. 1995). Values of  $\delta^{18}\text{O}$   
277 of whole rock powders (~2mg) of Dinkey Dome granite and Dinkey Creek sedimentary rocks  
278 were analyzed by laser fluorination using an airlock sample chamber (Spicuzza et al. 1998)  
279 (Supplementary Table E).

### 280 **SIMS analysis of $\delta^{18}\text{O}$ in garnet and zircon**

281 Oxygen isotope ratios were measured at the WiscSIMS Laboratory, Department of  
282 Geoscience, UW-Madison with a CAMECA ims-1280 large-radius multicollector ion  
283 microprobe/SIMS (Kita et al. 2009; Valley and Kita 2009). Oxygen isotopes were analyzed  
284 using a 2.0–2.2 nA primary  $\text{Cs}^+$  beam accelerated by 10 kV (impact energy = 20 kV) and  
285 focused on sample surface with ~10–12  $\mu\text{m}$  spot diameter. Secondary  $^{16}\text{O}$  and  $^{18}\text{O}^-$  ions were  
286 measured by two Faraday cup detectors simultaneously. Zircon standard KIM-5 ( $\delta^{18}\text{O} = 5.09 \text{ ‰}$   
287 VSMOW; Valley 2003) and garnet standard UWG-2 ( $\delta^{18}\text{O} = 5.80 \text{ ‰ VSMOW}$ ; Valley et al.  
288 1995) were mounted in the center of each sample and used as running standards to bracket  
289 unknown sample analyses. Four consecutive measurements of the standard were made before  
290 and after every set of 10 sample analyses. Additional standardization and calibration of garnet  
291 standards was performed to account for the compositional effects on instrumental bias as  
292 described previously (Page et al. 2010, Russell et al. 2013, Kitajima et al. 2016). Typically, two  
293 analysis spots were made on each zircon (core and rim), and approximately 3-8 spots (rim to  
294 rim) on each garnet.

295 Cracks, inclusions, radiation-damaged zircon domains and other features that can  
296 compromise an analysis were avoided by secondary electron (SE), backscattered electron (BSE),  
297 and cathodoluminescence (CL) imaging of minerals before in situ analysis. In addition, all SIMS

298 pits were imaged post-analysis using BSE and SE, and pits that hit cracks or contain mineral  
299 inclusions are culled from the final dataset (Supplementary Tables C-D).

### 300 **SIMS analysis of REEs in zircon**

301 Zircon grains were analyzed by SIMS for trace elements, including rare earth elements  
302 (REEs) in the WiscSIMS Laboratory at UW-Madison with a CAMECA ims-1280. The following  
303 elements were analyzed: Li, Si, P, Ca, Ti, V, Fe, Y, La, Ce, Pr, Nd, Sm, Eu, Tb, Gd, Dy, Ho, Er,  
304 Tm, Yb, Lu, Hf, Th, and U (Supplementary Table F). Similar conditions as Page et al. (2007b)  
305 were used: impact energy of 23 kV, 4 nA O<sup>-</sup> ion beam shaped to a diameter of 25 μm on the  
306 sample surface and a secondary ion accelerating voltage of 10 kV. For trace element analysis the  
307 configuration of the secondary ion optics was optimized for high transmission (Kita et al. 2009).  
308 A single electron multiplier, field aperture of 4000 μm, MRP of 3000, and secondary beam  
309 energy offset of 40 V were used and allow resolution of the selected REE peaks from the  
310 interfering REE oxides. Measured counts for each element were normalized to <sup>30</sup>Si. During the  
311 analysis session, NIST-610 glass was used as a running standard. To estimate the matrix effects  
312 on relative sensitivity factor (RSF) between zircon and NIST 610, the zircon standards 91500 (Y,  
313 REE, Hf, Th and U: Wiedenbeck et al. 2004) and Xinjiang (Li: Ushikubo et al. 2008) were  
314 analyzed at the beginning of the trace element session. For Ti concentration, we used the  
315 correction factor on RSF between zircon and NIST-610 reported by Fu et al. (2008). No  
316 correction for matrix effect was applied on P, Ca, V and Fe because their concentrations in the  
317 91500 zircon are unknown. Counting times were adjusted for NIST-610 because of the  
318 difference in REE composition in comparison to natural zircons (Page et al. 2007b)  
319 (Supplementary Table F).

### 320 **Results**

321 **Garnet composition by EPMA**

322 Garnet grains from the Dinkey Dome pluton are almandine-spessartine-rich with minor  
323 pyrope and grossular ( $X_{\text{Alm}} = 0.60\text{-}0.86$ ;  $X_{\text{Sps}} = 0.11\text{-}0.27$ ;  $X_{\text{Pyp}} = 0.01\text{-}0.07$ ;  $X_{\text{Grs}} = 0.02\text{-}0.06$ )  
324 (Fig. 5a). Most of the garnets analyzed in this study slightly increase in spessartine and decrease  
325 in almandine at the rims. Internal cation zoning is generally subtle, however crystals 1S52-02,  
326 1S52-04, 1S80-04, and 10DD07b-02 show bell-shaped rim-to-rim profiles. Compositionally,  
327 garnet is similar to garnet from other Sierran granitoids (Guy and Wones 1980, Calk and Dodge  
328 1986, Ague and Brimhall 1988a, Liggett 1990; Lackey et al. 2006). Values of  $X_{\text{Grs}}$  are higher in  
329 western side of the pluton, suggesting slightly higher crystallization pressures. Crystals from the  
330 eastern side of the pluton have less pyrope and are generally more almandine-rich (Fig. 5a),  
331 which can explain the difference in color east to west.

332 **Oxygen isotope ratios by Laser Fluorination**

333 Laser fluorination analyses of oxygen isotope ratios in garnet from a west to east traverse  
334 (A-A', Fig. 2 and 6) were conducted to assess variations between pink garnet (lower  $X_{\text{Alm}}$ ) and  
335 red garnet. Only one of the samples analyzed (1S51) shows a variation in  $\delta^{18}\text{O}$  between red ( $7.25$   
336  $\pm 0.23\%$  2SD) and pink garnet ( $6.80 \pm 0.23\%$ ); the other samples showing different color grains  
337 (1S77, 1S79, and 1S82) show no variation in  $\delta^{18}\text{O}$ .

338 Individual garnets from samples 1S51, 1S52, 1S53, 1S77, 1S79, 1S80, and 1S81 were  
339 handpicked and analyzed by both laser fluorination and SIMS (Supplementary Table E). Values  
340 of  $\delta^{18}\text{O}$  obtained by laser fluorination for these grains average  $6.90 \pm 0.18\%$  (1SD) for the eastern  
341 side and  $7.63 \pm 0.17\%$  to the west. These values are similar to those obtained Lackey et al.  
342 (2006), who also reported lower  $\delta^{18}\text{O}$  for garnet from the eastern part of the pluton.

343 Whole rock analyses were also made of granite and metasediment samples 10DD-02  
344 through 10DD-22 (Table 1). The granite  $\delta^{18}\text{O}(\text{WR})$  values range from 9.0 to 10.5‰, and the  
345 metasedimentary rocks (biotite hornfels and quartzite) range in  $\delta^{18}\text{O}(\text{WR})$  from 11.7 to 12.8‰.

#### 346 **Oxygen isotope ratios by SIMS**

347 **Garnet.** Garnets from the western side of the pluton analyzed by SIMS resemble the  
348 laser fluorination analysis (within uncertainty). In contrast, garnets from the eastern side of the  
349 pluton show consistently lower values relative to laser fluorination analysis, with a difference of  
350  $\delta^{18}\text{O}$  values ranging from 0.6 to 1.5‰ (Fig. 6b) (Table 1). These differences likely result from  
351 quartz inclusions within garnet crystals that are higher in  $\delta^{18}\text{O}$  and were unavoidably analyzed by  
352 laser fluorination. The SIMS analyses avoid inclusions that are plainly visible in polished  
353 surfaces and thus SIMS values of  $\delta^{18}\text{O}$  are not affected by inclusions.

354 Values of  $\delta^{18}\text{O}$  in epoxy-mounted garnet grains from western side of the pluton are  
355 higher (average  $\delta^{18}\text{O}(\text{Grt}) = 7.4 \pm 0.2\text{‰}$ ) than eastern side  $\delta^{18}\text{O}(\text{Grt})$  values of  $6.3 \pm 0.2\text{‰}$ , and  
356 show no significant core to rim zoning in  $\delta^{18}\text{O}$ . Average values of  $\delta^{18}\text{O}$  measured from garnets  
357 selected in thin section show a similar trend with higher values on the western side ( $6.9 \pm 0.3\text{‰}$ )  
358 and lower values on the eastern side ( $5.2 \pm 0.3\text{‰}$ ). However, unlike garnet hand-picked from  
359 mineral separates, garnets in thin section show variation in  $\delta^{18}\text{O}$  from rims to cores (Fig.7). The  
360 core to rim variation is more prominent on the larger ( $>1$  mm) garnets from the northwestern side  
361 of the pluton. The zoning of the eastern-side garnets is more subtle and less common (Table 1).

362 This difference likely results due to analysis of larger subhedral garnets in thin section  
363 rather than the smaller equant garnets that were selected from mineral separates. It is also  
364 possible that the low  $\delta^{18}\text{O}$  garnets are more delicate and were destroyed by the disk mill during  
365 sample processing. The  $\delta^{18}\text{O}$  in garnets from thin sections on the east side is very low (ave. = 5.2



366  $\pm 0.3\%$ ). This pattern, combined with the observation of large miarolitic cavities in the east side  
367 of the pluton suggests the possibility of the garnet rims growing into the sub-solidus realms, with  
368 some non-magmatic water infiltrating the system. Studies of Cretaceous skarns in the south-  
369 central Sierra show that garnet growing in shallow hydrothermal systems may record multiple  
370 episodes of fluid flow and low- $\delta^{18}\text{O}$  domains record incursions of meteoric water at different  
371 times, including waning stages of garnet growth (e.g., D'Errico et al. 2012; Ryan-Davis et al.  
372 2019). Therefore, the Dinkey Dome garnet may record some surface water infiltration on the  
373 East side.

374 **Zircon.** SIMS analyses of rims and cores of individual zircon grains from 10 Dinkey  
375 Dome samples along the A-A' traverse (Fig. 2, 1S51-1S82) show constant  $\delta^{18}\text{O}$  values for the  
376 cores:  $7.8 \pm 0.3\%$  on the east side and  $7.7 \pm 0.3\%$  on the west side. The rims of the zircons have  
377 consistently lower  $\delta^{18}\text{O}$  values that average  $6.7 \pm 0.3\%$  on the east side and  $6.9 \pm 0.3\%$  on the  
378 west side (Fig. 6a).

379 SIMS  $\delta^{18}\text{O}$  values of zircon in thin sections from the eastern side average  $7.2 \pm 0.2\%$   
380 (Fig. 6a, Table 1). The average  $\delta^{18}\text{O}$  in each zircon from the western part of the pluton is  $7.6$   
381  $\pm 0.2\%$ . These values are consistent with SIMS data for zircon cores ( $7.7$  to  $7.8\%$ ) that dominate  
382 the mass of each zircon. Zircons from some samples (10DD-02a-b, 10DD-05a, 10DD-16c,  
383 10DD-17, and 10DD-19c) did not have rims that were distinguishable by CL.

#### 384 **Trace elements in zircon**

385 Trace element compositions in cores and rims of grains from the Dinkey Dome granite  
386 are summarized in chondrite-normalized REE diagrams (Fig. 8). The REE data are consistent  
387 with igneous zircon from continental crust (Belousova et al. 1998; Hoskin and Ireland 2000;

388 Belousova et al. 2002, Grimes et al. 2007) and show HREE enrichment, a positive Ce anomaly  
389 and a negative Eu anomaly (Fig. 8).

390 All zircon data plot within the ‘magmatic’ field in REE discriminant diagrams:  $(\text{Sm}/\text{La})_{\text{N}}$   
391 vs. La (ppm) and  $\text{Ce}/\text{Ce}^*$  ( $(\text{Ce})_{\text{N}}/\sqrt{((\text{La})_{\text{N}}(\text{Pr})_{\text{N}})}$  vs.  $(\text{Sm}/\text{La})_{\text{N}}$  (Figs. 9a and b). None of the cores  
392 or rims have REE compositions similar to hydrothermal zircon (Hoskin 2005). Although  
393 Chondrite normalized REE patterns are similar in cores and rims of grains (Fig. 8),  $(\text{Sm}/\text{La})_{\text{N}}$  vs.  
394 La (ppm) and  $\text{Ce}/\text{Ce}^*$  vs.  $(\text{Sm}/\text{La})_{\text{N}}$  are clearly bimodal, with rims having slightly flatter LREEs  
395 and being higher in [La] and lower  $(\text{Sm}/\text{La})_{\text{N}}$ , (Figs. 9a and 9b).

## 396 Discussion

### 397 Causes of $\delta^{18}\text{O}$ zoning

398 The in situ measurements of  $\delta^{18}\text{O}$  and trace elements from magmatic garnet and zoned  
399 zircon grains reveal a more complex magmatic history of assimilation and fractional  
400 crystallization for the Dinkey Dome granite than was resolved by bulk-mineral analysis. High-  
401  $\delta^{18}\text{O}$  zircon cores crystallized from an initially high- $\delta^{18}\text{O}$  magma derived by melting of a high-  
402  $\delta^{18}\text{O}$  source deeper in the crust (Figs. 10 and 11). The zircon cores average 7.7‰, indicating  
403  $\delta^{18}\text{O}(\text{magma})$  values of 9.4‰ [ $\sim 69$  wt. %  $\text{SiO}_2$ ;  $\Delta^{18}\text{O}(\text{WR-Zrc}) \approx 0.0612$  (wt.%  $\text{SiO}_2$ ) – 2.5‰  
404 (Lackey et al. 2008)]. The inclusions of zircon in garnet and the steep positive slope of HREEs in  
405 zircon indicate that the majority of garnet grew after zircon. Lower  $\delta^{18}\text{O}$  values in the rims of  
406 zircon (ave. 6.8‰) and throughout most garnets show that a lower  $\delta^{18}\text{O}$  contaminant, possibly  
407 hydrothermally altered rocks, contributed some low- $\delta^{18}\text{O}$  melt into parts of the magma at depth.  
408 Quartz from the Dinkey Dome and whole rocks (including feldspars) do not record such low  
409  $\delta^{18}\text{O}$  values (Lackey et al. 2006), however absence of low- $\delta^{18}\text{O}$  values in quartz and feldspar  
410 could arise from exchange of oxygen isotopes between these minerals with igneous fluids

411 contributed from younger, more voluminous magmas (e.g., the 101 Ma Dinkey Creek  
412 Granodiorite) that engulfed the Dinkey Dome pluton and its aureole. The assimilation and  
413 fractional crystallization history of Dinkey Dome magma thus appears preferentially preserved in  
414 zircon and garnet due to the minerals' slower diffusion rates relative to quartz and feldspar.

415 It is significant that no low  $\delta^{18}\text{O}$  (< 5‰) rocks are identified in the pendant immediately  
416 adjacent to the Dinkey Dome pluton. Thus, the lower  $\delta^{18}\text{O}$  domains in garnet and zircon point to  
417 this stage of melting and contamination of the magma at depths greater than final crystallization  
418 depths. The wallrock in the Sierran arc is heterogeneous by nature, containing domains of  
419 Triassic and Jurassic hydrothermally altered volcanic wallrocks with relatively low  $\delta^{18}\text{O}$  (e.g.,  
420 Peck and Van Kooten 1983; D'Errico et al. 2012; Ryan-Davis et al. 2019). Such metavolcanic  
421 and metasedimentary wallrocks are the most likely source of a low- $\delta^{18}\text{O}$  assimilation signature.  
422 Evidence of melting is found where migmatite complexes are developed in metavolcanics rocks  
423 at mid- to lower-crustal level pendants in the southern Sierra Nevada (Saleeby et al. 2003).  
424 Nevertheless, thermal budgets of peraluminous magma should limit significant melting and  
425 assimilation of wallrock at emplacement levels of the Dinkey Dome pluton, or mixing of  
426 magmas, thus the low- $\delta^{18}\text{O}$  assimilation may be restricted to a thin veneer of the eastern half of  
427 the pluton, where garnets record the lowest  $\delta^{18}\text{O}$  values. The eastern part is also at a higher  
428 elevation, and thus it is possible the isotopic signatures are restricted to a thin copula (Fig. 11),  
429 and/or that the isotopic signatures of the eastern side are correlative to rocks eroded away from  
430 the western side. Discrete zoning is shown by the heterogeneous nature of the Dinkey Dome  
431 pluton; the northwestern samples show a rim-ward shift to higher  $\delta^{18}\text{O}$  in some garnet rims  
432 suggesting that as some of the magma was produced and transported, it encountered high- $\delta^{18}\text{O}$   
433 rock and was locally contaminated (Fig. 11).

434 **Episodic contamination of a peraluminous magma**

435       The findings from this work also raise the question of how, given their small size and  
436 limited thermal budgets, high silica magmas may episodically interact with wallrocks in arc  
437 crust. This process is partially illustrated at the pluton scale by the Hall Canyon pluton in the  
438 Panamint Range, California (Mahood et al. 1996). Here, a roof zone with pegmatitic and aplitic  
439 domains is enriched in peraluminous minerals (garnet, muscovite) compared to lower in the  
440 pluton, however the entire pluton is peraluminous. The authors invoke in situ fractionation of the  
441 magma in the upper roof zone with additional melts also percolating up into the roof zone from  
442 the lower reaches of the pluton. In such a scenario, fractionating melt increases peraluminosity  
443 (such as seen in the eastern Dinkey Dome pluton) and promotes additional growth of  
444 peraluminous minerals (e.g. garnet, sillimanite, and andalusite). Because fractionating  
445 peraluminous magmas sees increased concentrations of water and incompatible elements, this  
446 fractionation would counteract the tendency of cooling and crystallization to impede distribution  
447 of new melt into the “mushy” roof zone of the pluton (e.g., Scaillet et al. 2000). A similar  
448 process might have occurred in the eastern Dinkey Dome pluton whereby a more highly  
449 fractionated roof zone continued to receive melts and consequently achieved the isotopic  
450 heterogeneity seen in crystal-scale  $\delta^{18}\text{O}$  zoning that was not recorded in the western domain.  
451 Sustained melt and fluid percolation in the east side also could have allowed low- $\delta^{18}\text{O}$  values to  
452 be recorded in some generations of garnet that continued to grow as peraluminosity increased. In  
453 contrast, the west side of the pluton crystallized deeper and relatively earlier and thus did not  
454 record incorporation of the low- $\delta^{18}\text{O}$  material and thus was more homogeneous in its  
455 composition. Thus, the east and west sides of the Dinkey Dome pluton behaved as two magma  
456 batches, separated by a septum of metasediments, that accumulated, fractionated, and ultimately

457 crystallized.

458 **Timing and preservation of crustal melts in arcs**

459       Given that the Dinkey Dome pluton was emplaced into its pendant rocks earlier than other  
460 plutons in the Shaver Intrusive suite, it would have been emplaced inboard of the main locus of  
461 magmatism in the arc, and likely encountered a thicker, more heterogeneous crustal column and  
462 interactions with that crust superimposed additional contamination on the magma. The Dinkey  
463 Dome is not the only example in the region. The Grant Grove peraluminous granite, which  
464 shares similarities with Dinkey Dome, like being isolated by pendant rocks and surrounded by  
465 younger metaluminous plutons, shows higher  $\delta^{18}\text{O}$  in its margin indicative of localized  
466 contamination (Lackey et al. 2006). That localized “vener” of later contamination is manifested  
467 by additional growth of garnet and aluminosilicates at the margin of the pluton where it intruded  
468 and partially melted schists near emplacement levels.

469       Although of Jurassic age, peraluminous plutons that intrude the Julian Schist in the  
470 Peninsular Ranges batholith in southern California are comparable (Shaw et al. 2003). These  
471 granites are relatively small compared the younger (Cretaceous) tonalite and granodiorite plutons  
472 that surround them, comprising most of the Peninsular Ranges batholith. Some of the Jurassic  
473 plutons are directly associated with migmatitic zones in the Julian Schist and have elevated  $\text{Sr}_i$   
474 ( $>0.71$ ) and  $\delta^{18}\text{O}$  (16-20‰), values that overlap with the schist itself indicating it was the source  
475 of the melts that produced the peraluminous plutons. Though of much greater age difference than  
476 the Dinkey Dome and younger plutons that surround it and associated pendant rocks, the  
477 progression from early, small peraluminous plutons to larger metaluminous plutons is the same.  
478 Unlike the Peninsular Ranges example, the Dinkey Dome does not have evidence of a localized  
479 migmatite complex, consistent with its final shallow (low pressure) emplacement, although there

480 is evidence produced of migmatite complexes in lower crustal exposures in the Sierra (Zeng et  
481 al. 2005). In addition, the peraluminous plutons of the Peninsular Ranges contain abundant,  
482 Proterozoic zircon cores and crystals (Shaw et al. 2003), likely because melts from which they  
483 crystallized were saturated in zirconium and unable to dissolve grains inherited from their  
484 metasedimentary sources (e.g., Miller et al. 2003). The Dinkey Dome granite contains few  
485 inherited cores (Fig. 4). It follows is that the Dinkey Dome magmas were potentially derived  
486 from hotter or inheritance-poor sources (Miller et al. 2003) and presumably are farther separated  
487 from said source(s) that might be analogous to those in migmatite complexes in the southern  
488 Sierra (Zeng et al. 2005).

489 Overall, a theme emerges from the Mesozoic arc segments in California, wherein small  
490 volume peraluminous melts are the primary archive of melts of crustal “character,” but that these  
491 melts are restricted to earlier magmatism. It follows that because these antecedent magmas form  
492 in early stages of magmatism, as heat content in the arc is ramping, they may have sustained  
493 mobility, which allows them to preserve more chemical heterogeneity. The increased vigor of arc  
494 magmatism also means that such crustal melt expression is muted in younger arc plutons. These  
495 later stages are typified by periods of high-flux magmatism from more organized sources that  
496 efficiently homogenize magmas with greater proportions of mantle melts (Lackey et al. 2012).

### 497 **Conclusions and Implications**

498 Contrasting records of isotopic heterogeneity in zircon and garnet crystals within  
499 different domains of the Dinkey Dome pluton exemplify how: 1) Sierran felsic granitoids  
500 originate though a variety of processes and are not restricted to end member models; and 2)  
501 early-stage plutons record crustal melting in the nascent stages of arc magmatism. The evolution  
502 of early-stage Sierran granitoids reflects intermediate processes whereby magmas became more

503 felsic due to a combination of processes such as contamination, assimilation and fractional  
504 crystallization at different stages (Lackey et al., 2005, 2006, 2008; Nelson et al. 2013). The  
505 requirement for an enriched-mantle model whereby granites are derived solely by several stages  
506 of partial melting and fractionation of these enriched-mantle sources, with no crustal input  
507 (Coleman and Glazner 1997; Ratajeski et al. 2001, 2005), need not be so restrictive given the  
508 high oxygen isotopic values recorded in cores of zircon grains ( $\delta^{18}\text{O} = 7.7$  to  $7.8\%$ ) in the Dinkey  
509 Dome pluton. Instead, before an arc organizes a Melting-Assimilation-Storage-and  
510 Homogenization (MASH) system, hot zone (Annen et al. 2006), or similar magmatic source  
511 region capable of homogenizing unusual melt compositions, peraluminous plutonic “harbingers”  
512 like Dinkey Dome sample the pre-batholithic crustal structure. This crustal melt sampling period  
513 is brief and rare, but may be echoed in later stages arc stages when tectonic adjustments to the  
514 arc reposition crustal rocks into sites of melting (e.g., DeCelles et al. 2009), but also created  
515 conditions that are favorable to preserve such melts in structurally and thermally isolated regions  
516 of arcs such as in shear zones and metamorphic wallrock complexes. As a case in point, the shut-  
517 down of the Sierran arc is accompanied by a structural disruption of the arc and introduction of  
518 fertile schists into the subduction channel that are expressed as late stage, small-volume, high  
519  $\delta^{18}\text{O}$  peraluminous melts (Chapman et al. 2013). Other intervals, such as during a major re-  
520 organization within the arc at 105 Ma saw an increase in  $\delta^{18}\text{O}$  and  $^{87}\text{Sr}/^{86}\text{Sr}$  consistent with a  
521 crustal melting episode (Holland et al. 2013). Thus, peraluminous plutons in arcs, though small  
522 and temporally restricted, record important aspects of the greater tectono-magmatic feedback  
523 systems and can potentially be used to identify cryptic crustal end members that become greatly  
524 diluted in more vigorous stages of arc magmatism produce the typical voluminous granodiorite.  
525

526

### Acknowledgements

527 The authors thank Noriko Kita and the WiscSIMS group for SIMS analysis, John Fournelle  
528 for EPMA, Mike Spicuzza for laser fluorination, Brian Hess for polishing samples, and Adam  
529 Kinnard for help in the field. We also thank Chris Harris and an anonymous reviewer for  
530 constructive and detailed reviews that improved the paper, and William Peck for editorial  
531 comments. This study was supported by a BP plc–University of Wisconsin Research  
532 Assistantship, the DOE 93ER14389 and NSF EAR-0838058 (JWV), and NSF EAR-0948706  
533 (JSL). WiscSIMS is supported by National Science Foundation (EAR-1658823) and the  
534 University of Wisconsin – Madison.

535

### References

536 Ague, J.J., and Brimhall, G.H. (1988a) Regional variations in bulk chemistry, mineralogy, and  
537 the compositions of mafic and accessory minerals in the batholiths of California. Geological  
538 Society of America Bulletin, 100, 891–911.

539 Ague, J.J., and Brimhall, G.H. (1988b) Magmatic arc asymmetry and distribution of anomalous  
540 plutonic belts in the batholiths of California: effects of assimilation, crustal thickness, and  
541 depth of crystallization. Geological Society of America Bulletin, 100, 912–927.

542 Ardill, K., Paterson, S., and Memeti, V. (2018) Spatiotemporal magmatic focusing in upper-mid  
543 crustal plutons of the Sierra Nevada arc. Earth and Planetary Science Letters, 498, 88–100.

544 Annen, C., Blundy, J.D., and Sparks, R.S.J. (2006) The genesis of intermediate and silicic  
545 magmas in deep crustal hot zones: Journal of Petrology, 47, 505–539.

546 Barnes, C.G., Berry, R., Barnes, M.A., Ernst, W.G. (2017) Trace element zoning in hornblende:  
547 tracking and modeling the crystallization of a calc-alkaline arc pluton. American  
548 Mineralogist, 102, 2390–2405.



- 549 Bateman, P.C. (1992) Plutonism in the central part of the Sierra Nevada batholith, California.  
550 USGS Professional Paper, 1483, 186 p.
- 551 Bateman, P.C., and Wones, D.R. (1972) Geologic map of the Huntington lake quadrangle,  
552 central Sierra Nevada, California. USGS Geologic Quadrangle Map 987.
- 553 Belousova, E.A., Griffin, W.L., and Pearson, N.J. (1998) Trace element composition and  
554 cathodoluminescence properties of southern African kimberlitic zircons. Mineralogical  
555 Magazine, 62, 355–366.
- 556 Belousova, E.A., Griffin, W.L., O'Reilly, S.Y., and Fisher, N.I. (2002) Igneous zircon: trace  
557 element composition as an indicator of source rock type. Contributions to Mineralogy and  
558 Petrology, 143, 602–622.
- 559 Bindeman, I.N. (2008) Oxygen Isotopes in Mantle and Crustal Magmas as Revealed by Single  
560 Crystal Analysis. Reviews in Mineralogy and Geochemistry, 69, 445–478.
- 561 Bowman, J.R., Moser, D.E., Valley, J.W., Wooden, J.L., Kita, N.T., and Mazdab, F.K. (2011)  
562 Zircon U-Pb isotope,  $\delta^{18}\text{O}$  and trace element response to 80 m.y. of high temperature  
563 formation. American Journal of Science, 311, 719–772.
- 564 Calk, L.C., and Dodge, F.C. (1986) Garnet in granitoid rocks of the Sierra Nevada Batholith,  
565 California. 14<sup>th</sup> International Mineralogical Association, Abstracts, p. 69.
- 566 Chapman, J.B., and Ducea, M.N. (2019) The role of arc migration in Cordilleran orogenic  
567 cyclicity. Geology, 47, 627–631.
- 568 Chapman, A.D., Saleeby, J.B., and Eiler, J. (2013) Slab flattening trigger for isotopic disturbance  
569 and magmatic flare-up in the southernmost Sierra Nevada Batholith, California. Geology,  
570 41(9), 1007-1010.

- 571 Chappell, B.W., and White, A.J.R. (1974) Two contrasting granite types. *Pacific Geology*, 8,  
572 173–174.
- 573 Chen J.H., and Moore J.G. (1982) Uranium-lead isotopic ages from the Sierra Nevada batholith,  
574 California. *Journal of Geophysical Research*, 87, 4761–4784.
- 575 Chin, E.J., Lee, C.T.A., and Barnes, J.D. (2014) Thickening, refertilization, and the deep  
576 lithosphere filter in continental arcs: Constraints from major and trace elements and oxygen  
577 isotopes. *Earth and Planetary Science Letters*, 397, 184-200.
- 578 Clarke, D.B., Dorais, M., Barbarin, B., Barker, D., Cesare, B., Clarke, G., El Baghdadi, M.,  
579 Erdmann, S., Forster, H.J., Gaeta, M., and others (2005) Occurrence and Origin of  
580 Andalusite in Peraluminous Felsic Igneous Rocks. *Journal of Petrology* 46, 441–472.
- 581 Clemens, J.D., and Wall, V.J. (1981) Origin and crystallization of some peraluminous (S-type)  
582 granitic magmas. *Canadian Mineralogist*, 19, 111–131.
- 583 Coleman, D.S., and Glazner, A.F. (1997) The Sierra Crest magmatic event: rapid formation of  
584 juvenile crust during the late Cretaceous in California. *International Geological Review*, 39,  
585 768–787.
- 586 Coleman, D.S., Gray, W., and Glazner, A.F. (2004) Rethinking the emplacement and evolution  
587 of zoned plutons: Geochronologic evidence for incremental assembly of the Tuolumne  
588 Intrusive Suite, California. *Geology*, 32, 433–436.
- 589 Coughlan, R.A. (1990) Studies in diffusional transport: grain boundary transport of O in  
590 feldspars, diffusion of O, strontium, and the REEs in garnet and thermal histories of granitic  
591 intrusions in south-central Maine using O isotopes, 476 p. Ph.D. thesis, Brown University,  
592 Providence.
- 593 Davis, J.W., Coleman, D.S., Gracely, J.T., Gaschnig, R., and Stearns, M. (2012) Magma

- 594 accumulation rates and thermal histories of plutons of the Sierra Nevada batholith, CA.  
595 Contributions to Mineralogy and Petrology, 163, 449–465.
- 596 DeCelles, P.G., Ducea, M.N., Kapp, P., and Zandt, G. (2009) Cyclicity in Cordilleran orogenic  
597 systems. Nature Geoscience, 2, 251-257.
- 598 D'Errico, M.E., Lackey, J.S., Surpless, B.E., Loewy, S.L., Wooden, J.L., Barnes, J.D.,  
599 Strickland, A., and Valley, J.W. (2012) A detailed record of shallow hydrothermal fluid flow  
600 in the Sierra Nevada magmatic arc from low- $\delta^{18}\text{O}$  skarn garnets. Geology, 40, 763–766.
- 601 Dorais, M.J., Whitney, J.A., and Roden, M.F. (1990) Origin of Mafic Enclaves in the Dinkey  
602 Creek Pluton, Central Sierra Nevada Batholith, California. Journal of Petrology, 31, 853–  
603 881.
- 604 Ducea, M.N. (2001) The California arc: Thick granitic batholiths, eclogitic residues,  
605 lithospheric-scale thrusting and magmatic flare-ups. Geological Society of America Today,  
606 11, 4–10.
- 607 Finch, J.R., Hanchar, J.M., Hoskin, P.W.O., and Burns, P.C. (2001) Rare-earth elements in  
608 synthetic zircon: Part 2. A single-crystal X-ray study of xenotime substitution. American  
609 Mineralogy, 86, 681–689.
- 610 Fliedner, M.M., Klemperer, S.L., and Christensen, N.I. (2000) Three-dimensional seismic model  
611 of the Sierra Nevada arc, California, and its implications for crustal and upper mantle  
612 composition. Journal of Geophysical Research, 105, 10899–10921.
- 613 Frazer, R.E., Lackey, J.S., and Valencia, V.A. (2008) New U-Pb zircon ages of the granites of  
614 the Dinkey Dome; reexamining the origins of the Shaver Intrusive Suite. Geological Society  
615 of America, Abstracts with programs, 41, pp 14.

- 616 Frost, B.R., Barnes, C.G., Collins, W.J., Arculus, R.J., Ellis, D.J., and Frost, C.D. (2001) A  
617 geochemical classification for granitic rocks. *Journal of Petrology*, 42, 2033–2048.
- 618 Fu, B., Page, F.Z., Cavosie, A.J., Fournelle, J., Kita, N.T., Lackey, J.S., Wilde, S.A., and Valley,  
619 J.W. (2008) Ti-in-zircon thermometry: applications and limitations. *Contributions to*  
620 *Mineralogy and Petrology*, 156, 197-215.
- 621 Glazner, A.F., and Miller, D.M. (1997) Late-stage sinking of plutons. *Geology*, 25, 1099-1102.
- 622 Grimes, C.A., John, B.E., Kelemen, P.B., Mazdab, F.K., Wooden, J.L., Cheadle, M.J., Hanghøj,  
623 K., and Schwartz, J.J. (2007) Trace element chemistry of zircons from oceanic crust: A  
624 method for distinguishing detrital zircon provenance. *Geology*, 35, 643–646.
- 625 Guy, R.E. (1980) The Dinkey Creek intrusive series, Huntington Lake Quadrangle, Fresno  
626 County, California, 125 p., MS thesis, Virginia Polytechnic Institute, Blacksburg.
- 627 Guy, R.E., and Wones, D.R. (1980) Petrology of the Dinkey Creek Intrusive Series, Huntington  
628 Lake Quadrangle, Fresno County, California. Geological Society of America, Abstracts with  
629 programs, 12, pp 440.
- 630 Halden, N.M., Hawthorne, F.C., Campbell, J.L., Teesdale, W.J., Maxwell, J.A., and Higuchi, D.  
631 (1993) Chemical characterization of oscillatory zoning and overgrowths in zircon using 3  
632 MeV  $\mu$ -PIXE. *Canadian Mineralogist*, 31, 637–647.
- 633 Halliday, A.N., Stephens, W.E., and Harmon, R.S. (1981) Isotopic and chemical constraints on  
634 the development of peraluminous Caledonian and Acadian granites. *Canadian Mineralogist*,  
635 19, 205–216.
- 636 Hinton, R.W., and Upton, B.G.J. (1991) The chemistry of zircon: variations within and between  
637 large crystals from syenite and alkali basalt xenoliths. *Geochimica et Cosmochimica Acta*,  
638 55, 3287–3302.

- 639 Holland, J.E., Surpless, B., Smith, D.R., Loewy, S.L., and Lackey, J.S. (2013) Intrusive history  
640 and petrogenesis of the Ash Mountain Complex, Sierra Nevada batholith, California (USA).  
641 *Geosphere*, 9, 691–717.
- 642 Hoskin, P.W.O. (2005) Trace-element composition of hydrothermal zircon and the alteration of  
643 Hadean zircon from the Jack Hills, Australia. *Geochimica et Cosmochimica Acta*, 69, 637–  
644 648.
- 645 Hoskin, P.W.O., and Ireland, T.R. (2000) Rare earth element chemistry of zircon and its use as a  
646 provenance indicator. *Geology*, 28, 627 – 630.
- 647 Hoskin, P.W.O., and Schaltegger, U. (2003) The composition of zircon and igneous  
648 metamorphic petrogenesis. *Reviews in Mineralogy and Geochemistry*, 53, 27–62.
- 649 Hoskin, P.W.O., Kinny, P.D., Wyborn, D., and Chappell, B.W. (2000) Identifying accessory  
650 mineral saturation during differentiation in granitoid magmas: an integrated approach.  
651 *Journal of Petrology*, 41, 1365–1396.
- 652 Jeon, H., Williams, I.S., and Chappell, B.W. (2012) Magma to mud to magma: rapid crustal  
653 recycling by Permian granite magmatism near the eastern Gondwana margin. *Earth and  
654 Planetary Science Letters*, 319-320, 104–117.
- 655 Kelly, J.L., Fu, B., Kita, N.T., and Valley, J.W. (2007) Optically continuous silcrete quartz  
656 cements of the St. Peter Sandstone: High precision oxygen isotope analysis by ion  
657 microprobe. *Geochimica et Cosmochimica Acta*, 71, 3812 – 3832.
- 658 King, E.M., and Valley, J.W. (2001) The source, magmatic contamination, and alteration of the  
659 Idaho batholith. *Contributions to Mineralogy and Petrology*, 142, 72–88.

- 660 Kistler, R.W. (1990) Two different lithosphere types in the Sierra Nevada, California. In: J.L.  
661 Anderson, Eds., The nature and origin of Cordilleran magmatism, Geological Society of  
662 America Memoir, 174, 271–281, Geological Society of America, Boulder.
- 663 Kistler, R.W., and Peterman, Z.E. (1973) Variations in Sr, Rb, K, Na, and Initial Sr87/Sr86 in  
664 Mesozoic Granitic Rocks and Intruded Wall Rocks in Central California. Geological Society  
665 of America Bulletin, 84, 3489–3512.
- 666 Kita, N.T., Ushikubo, T., Fu, B., and Valley, J.W. (2009) High Precision SIMS Oxygen Isotope  
667 Analyses and the Effect of Sample Topography. Chemical Geology, 264, 43–57.
- 668 Kitajima, K., Strickland, A., Spicuzza, M.J., Tenner, T.J., and Valley, J.W. (2016) Improved  
669 matrix correction of  $\delta^{18}\text{O}$  analysis by SIMS for pyralspite and Cr-pyropes garnets.  
670 Goldschmidt Conference, 1542, Yokohama, Japan.
- 671 Lackey, J.S., Valley, J.W., and Saleeby, J.B. (2005) Evidence from zircon for high- $\delta^{18}\text{O}$   
672 contamination of magmas in the deep Sierra Nevada batholith, California. Earth and  
673 Planetary Science Letters, 235, 315–330.
- 674 Lackey, J.S., Valley, J.W., and Hinke, H.J. (2006) Deciphering the source and contamination  
675 history of peraluminous magmas using  $\delta^{18}\text{O}$  of accessory minerals: examples from garnet-  
676 bearing plutons of the Sierra Nevada Batholith. Contributions to Mineralogy and Petrology,  
677 151, 20–44.
- 678 Lackey, J.S., Valley, J.W., Chen, J.H., and Stockli, D.F. (2008) Dynamic Magma Systems,  
679 Crustal Recycling, and Alteration in the Central Sierra Nevada Batholith: The Oxygen  
680 Isotope Record. Journal of Petrology. 49, 1397–1426.

- 681 Lackey, J.S., Erdmann, S., Hark, J.S., Nowak, R.M., Murray, K.E., Clarke, D.B., and Valley,  
682 J.W. (2011) Tracing garnet origins in granitoid rocks by oxygen isotope analysis: Examples  
683 from the South Mountain Batholith, Nova Scotia. *Canadian Mineralogist*, 49, 417–439.
- 684 Lackey, J.S., Cecil, M.R., Windham, C.J., Frazer, R.E., Bindeman I.N., and Gehrels, G. (2012)  
685 The Fine Gold Intrusive Suite: The Roles of Basement Terranes and Magma Source  
686 Development in the Early Cretaceous Sierra Nevada Batholith. *Geosphere*, 8, 292–313.
- 687 Lee, C.T., Cheng, X., and Horodyskyj, U. (2006) The development and refinement of continental  
688 arcs by primary basaltic magmatism, garnet pyroxenite accumulation, basaltic recharge and  
689 delamination: insights from the Sierra Nevada, California. *Contributions to Mineralogy and*  
690 *Petrology*, 151, 222 - 242.
- 691 Liggett, D.L. (1990) Geochemistry of the garnet bearing Tharps Peak Granodiorite and its  
692 relation to other members of the Lake Kaweah Intrusive Suite, southwestern Sierra Nevada,  
693 California In: J.L. Anderson, Eds., *The nature and origin of Cordilleran magmatism*,  
694 *Geological Society of America Memoir*, 174, 205-236.
- 695 Mahood, G.A., Nibler, G.E., and Halliday, A.N. (1996) Zoning patterns and petrologic processes  
696 in peraluminous magma chambers: Hall Canyon pluton, Panamint Mountains, California.  
697 *Geological Society of America Bulletin*, 108, 437–453.
- 698 Memeti, V., Paterson, S., Matzel, J., Mundil, R., and Okaya, D. (2010) Magmatic lobes as  
699 “snapshots” of magma chamber growth and evolution in large, composite batholiths: an  
700 example from the Tuolumne Intrusion, Sierra Nevada, CA, *Geological Society of America*  
701 *Bulletin*, 122, 1912–1931.
- 702 Miller, C.F., McDowell, S.M., and Mapes, R.W. (2003) Hot and cold granites? Implications of  
703 zircon saturation temperatures and preservation of inheritance. *Geology*, 31, 529–532.

- 704 Moore, J.G., and Dodge, F.C.W. (1980) Late Cenozoic volcanic rocks of the southern Sierra  
705 Nevada, California: Part I. Geology and Petrology summary. Geological Society of America  
706 Bulletin, 91, 515–518.
- 707 Nelson, W.R., Dorais, M.J., Christiansen, E.R., and Hart, G.L. (2013) Petrogenesis of Sierra  
708 Nevada plutons inferred from Sr, Nd, and O isotopic signatures of mafic igneous complexes  
709 in Yosemite Valley, California. Contributions to Mineralogy and Petrology, 165, 397–417.
- 710 O’Neil, J.R. and Chappell, B.W. (1977) Oxygen and hydrogen isotope relation in the Berridale  
711 batholith. Journal of the Geological Society, 133, 559–571.
- 712 Ortiz, D.M. (2010) Mineral inclusions in zircons: A tool for provenance analysis of sedimentary  
713 rocks, MS thesis, University of Wisconsin, Madison, pp.44.
- 714 Page, F.Z., Fu, B., Kita, N.T., Fournelle, J., Spicuzza, M.J., Schulze, D.J., Viljoen, F., Basei,  
715 M.A.S., and Valley, J.W. (2007a) Zircons from kimberlite: new insights from oxygen  
716 isotopes, trace element, and Ti in zircon thermometry. Geochimica et Cosmochimica Acta  
717 71, 3887–3903.
- 718 Page, F.Z., Ushikubo, T., Kita, N.T., Riciputi, L.R., and Valley, J.W. (2007b) High precision  
719 oxygen isotope analysis of picogram samples reveals 2- $\mu$ m gradients and slow diffusion in  
720 zircon. American Mineralogist, 92, 1772–1775.
- 721 Page, F.Z., Kita, N.T., and Valley, J.W. (2010) Ion microprobe analysis of oxygen isotopes in  
722 garnets of complex chemistry. Chemical Geology, 270, 9–19.
- 723 Patiño Douce, A.E., and Johnston, A.D. (1991) Phase equilibria and melt productivity in the  
724 pelitic system: implications for the origin of peraluminous granitoids and aluminous  
725 granulites. Contributions to Mineralogy and Petrology, 107, 202–218.



- 726 Peck, D.L., and Van Kooten, G. (1983) Merced Peak Quadrangle, Central Sierra Nevada,  
727 California-Analytic Data. US Geological Survey Professional Paper 1170-D, 29 p.
- 728 Ratajeski, K., Glazner, A.F., and Miller, B.V. (2001) Geology and geochemistry of mafic to  
729 felsic plutonic rocks in the cretaceous intrusive suite of Yosemite Valley, California.  
730 Geological Society of America Bulletin, 113, 1485–1602.
- 731 Ratajeski, K., Sisson, T.W., and Glazner, A.F. (2005) Experimental and geochemical evidence  
732 for derivation of the El Capitan Granite, California, by partial melting of hydrous  
733 gabbroic lower crust. Contributions to Mineralogy and Petrology, 149, 713–734.
- 734 Russell, A.K., Kitajima, K., Strickland, A., Medaris Jr., L.G., Schulze, D.J., and Valley, J.W.  
735 (2013) Eclogite-facies Fluid Infiltration: Constraints from  $\delta^{18}\text{O}$  Zoning in Garnet.  
736 Contributions to Mineralogy and Petrology, 165, 103–116.
- 737 Ryan-Davis, J., Lackey, J.S., Gevedon, M., Barnes, J.D., Lee, C.T., Kitajima, K., and Valley,  
738 J.W. (2019) Andradite skarn garnet records of exceptionally low  $\delta^{18}\text{O}$  values within an  
739 Early Cretaceous hydrothermal system, Sierra Nevada, CA. Contributions to Mineralogy  
740 and Petrology, 174, 68, 1–19.
- 741 Saleeby, J., Ducea, M., and Clemens Knott, D. (2003) Production and loss of high-density  
742 batholithic root, southern Sierra Nevada, California. Tectonics, 22.
- 743 Sawka, W.N., and Chappell, B.W. (1988) Fractionation of uranium, thorium and rare earth  
744 elements in a vertically zoned granodiorite: Implications for heat production distributions in  
745 the Sierra Nevada batholith. Geochimica et Cosmochimica Acta, 52, 1131–1143.
- 746 Scaillet, B., Whittington, A., Martel, C., Pichavant, H., and Holtz, F. (2000) Phase equilibrium  
747 constraints on the viscosity of silicic magmas II: implications for mafic-silicic mixing  
748 processes. Transactions of the Royal Society of Edinburgh-Earth Sciences, 91, 61-72.

- 749 Scaillet, B., Holtz, F., and Pichavant, M. (2016) Experimental Constraints on the Formation of  
750 Silicic Magmas. *Elements*, 12, 109-114.
- 751 Sisson, T.W., Ratajeski, K., Hankins, W.B. et al. (2005) Voluminous granitic magmas from  
752 common basaltic sources. *Contributions to Mineralogy and Petrology*, 148, 635–661
- 753 Shaw, S.E., Todd, V.R., and Grove, M. (2003) Jurassic peraluminous gneissic granites in the  
754 axial zone of the Peninsular Ranges, Southern California, in S. E. Johnson, S. R. Paterson, J.  
755 M. Fletcher, G. H. Girty, D. L Kimbrough., and B. A. Martin, Eds., *Tectonic evolution of*  
756 *northwestern Mexico and the Southwestern USA*, pp. 157–183, Geological Society of  
757 America Special Paper, Boulder, Colorado.
- 758 Speer, J.A. (1982) Zircon. *Reviews in Mineralogy*, 5, 67–112.
- 759 Spicuzza, M.J., Valley, J.W., and McConnell, V.S. (1998) Oxygen isotope analysis of whole  
760 rock via laser fluorination: an air-lock approach. *Geological Society of America, Abstracts*  
761 *with programs*, 30, 80.
- 762 Taylor, H.P. and Sheppard, S.M.F. (1986) *Igneous Rocks: 1. Processes of Isotopic Fractionation*  
763 *and Isotope Systematics*. *Reviews in Mineralogy and Petrology*, 16, 227–272.
- 764 Tobisch, O.T., Renne, P.R., and Saleeby, J.B. (1993) Deformation resulting from regional  
765 extension during pluton ascent and emplacement, central Sierra Nevada, California. *Journal*  
766 *of Structural Geology*, 15, 609–628.
- 767 Tobisch, O.T., Fiske, R.S., Saleeby, J.B., Holt, E., and Sorensen, S.S. (2000) Steep tilting of  
768 metavolcanic rocks by multiple mechanisms, central Sierra Nevada, California. *Geological*  
769 *Society of America Bulletin*, 112, 1043-1058.

- 770 Ushikubo, T., Kita, N.T., Cavosie, A.J., Wilde, S.A., Rudnick, R.L., and Valley, J.W. (2008)  
771 Lithium in Jack Hills zircons: Evidence for extensive weathering of Earth's earliest crust.  
772 Earth and Planetary Science Letters, 272, 666–676.
- 773 Valley, J.W. (2003) Oxygen isotopes in zircon. Reviews in Mineralogy and Geochemistry, 53,  
774 343–385.
- 775 Valley, J.W., and Kita, N.T. (2009) In situ Oxygen Isotope Geochemistry by Ion Microprobe. In  
776 M. Fayek M., Eds., MAC Short Course: Secondary Ion Mass Spectrometry in the Earth  
777 Sciences, 41, 19–63.
- 778 Valley, J.W., Kitchen, N.E., Kohn, M.J., Niendorf, C.R., and Spicuzza, M.J. (1995) UWG-2, A  
779 garnet standard for oxygen isotope ratio: strategies for high precision and accuracy with laser  
780 heating. Geochimica et Cosmochim Acta, 59, 5223–5231.
- 781 Valley, J.W., Lackey, J.S., Cavosie, A.J., Clechenko C.C., Spicuzza M.J., Basei M. A. S.,  
782 Bindeman, I., Ferreira V., Sial A. N., King E. M., Peck W. H., Sinha A. K., and Wei C. S.  
783 (2005) Contributions to Mineralogy and Petrology, 150, 561–580.
- 784 Vielzeuf, D., Veschambre, M., and Brunet, F. (2005) Oxygen isotope heterogeneities and  
785 diffusional profiles in composite metamorphic/magmatic garnets from the Pyrenees.  
786 American Mineralogist, 90, 462–472.
- 787 Villaros, A., Stevens, G., Moyon, J.F., and Buick, I.S. (2009) The trace element compositions of  
788 S-type granites: evidence for disequilibrium melting and accessory phase entrainment in the  
789 source. Contributions to Mineralogy and Petrology, 158, 543–561.
- 790 Watson, E.B., and Cherniak, D.J. (1997) Oxygen diffusion in zircon. Earth and Planetary  
791 Science Letter, 148, 527–544.

- 792 Wenner J.M, and Coleman, D.S. (2004) Magma mixing and Cretaceous crustal growth: geology  
793 and geochemistry of granites in the central Sierra Nevada Batholith, California. International  
794 Geology Review, 46, 880-903.
- 795 Wiedenbeck, M., Hanchar, J.M., Peck, W.H., Sylvester, P., Valley, J.W., Whitehouse, M., Kronz  
796 A., Morishita, Y., Nasdala, L., Fiebig, J., and others (2004) Further Characterisation of the  
797 91500 Zircon Crystal. Geostandards and Geoanalytical Research, 28, 9–39.
- 798 Wones, D.R., Hon, R., and Bateman, P.C. (1969) Depth of crystallization of a garnet-bearing  
799 quartz monzonite of the Sierra Nevada Batholith. Eos Transactions, American Geophysical  
800 Union, 50, 329.
- 801 Wright, K., Freer, R., Catlow, C.R.A. (1995) Oxygen diffusion in grossular and some geological  
802 implications. American Mineralogist, 80, 1020–1025.
- 803 Zen, E. (1988) Phase relations of peraluminous granitic rocks and their petrogenetic  
804 implications. Annual Reviews in Earth and Planetary Science, 16, 21–51.
- 805 Zeng, L., Ducea, M., and Saleeby, J.B. (2005) Geochemical characteristics of crustal anatexis  
806 during the formation of migmatite at the southern Sierra Nevada, California. Contributions to  
807 Mineralogy and Petrology, 150, 386–402.

808 **List of figure captions**

- 809 Figure 1. Generalized map of the Central Sierra Nevada region, showing the location of  
810 peraluminous plutons and the study area, Dinkey Dome granite. Initial  $^{87}\text{Sr}/^{86}\text{Sr}=0.706$  and  
811 PA/NA= Panthalassan/North American Break from Kistler (1990). The high  $\delta^{18}\text{O}(\text{Zrn})$  (6.5-  
812 7.5‰) and low  $\delta^{18}\text{O}(\text{Zrn})$  (5.5-6.5‰) domains of the central Sierra Nevada intrusives are  
813 modified from Lackey et al. (2006, 2008).

814 Figure 2. Geologic map of the Dinkey Dome with sample sites from this study and Lackey et al.  
815 (2006). Map after Bateman and Wones (1972).

816 Figure 3. Garnet and associated minerals in the Dinkey Dome granite. Sample 10DD02a.  
817 Images a and b were taken under transmitted light (PPL= Plain polarized light, XPL= Cross  
818 polarized light). Image c is a backscattered electron image (BSE) and shows quartz, muscovite,  
819 apatite, ilmenite and zircon, included in a typical garnet from the Dinkey Dome pluton. Values  
820 of  $\delta^{18}\text{O}$  for this garnet are shown in Fig. 7.

821 Figure 4. Cathodoluminescence (CL) images of zircon grains from grain mounts 1S51-1S82  
822 (Transect A-A' Fig. 2). Circles represent SIMS spots and numbers represent oxygen isotope  
823 ratios ( $\delta^{18}\text{O}$ ). SIMS spots are 10  $\mu\text{m}$ ; scale bars are 50 $\mu\text{m}$ .

824 Figure 5. Cation composition of garnet phenocrysts from grain mounts and thin sections. (a)  
825 Almandine–spessartine–pyrope ternary plot includes garnet from both sides of the Dinkey  
826 Dome, showing that east side garnet is closer to the almandine-spessartine binary than garnet  
827 from the western half. (b) Representative rim-to-rim zoning profiles through the cores of garnets  
828 from samples 10DD06b-05 (west) and 10DD19c-02 (east). Background information for data  
829 presented in this figure can be found in supplementary data table B.

830 Figure 6. Oxygen isotope ratios in zircon (a) and garnet (b), and (c)  $\Delta 18\text{O}$  ( $\text{Grt}_{\text{Ave}} - \text{Zrc}_{\text{Ave}}$ ) from a  
831 traverse of the Dinkey Dome pluton (A-A' in Fig. 2) measured by ion microprobe (this study)  
832 and laser fluorination data of Lackey et al. (2006). Data represents zircon and garnet from grain  
833 mounts (1S51-1S82) and thin sections (10DD-02-10DD-19). Samples on x-axis are spaced  
834 according to relative distance of their field localities. See figure 2 for sample localities.  
835 Background information for data presented in this figure can be found in supplementary data  
836 tables A, C-D.

837 Figure 7. Example of a rim-rim traverse of oxygen analyses for a single garnet (10DD-02a-13,  
838 BSE image in thin section, see Fig. 3) measured by SIMS. Note the image is rotated  $\sim 90^\circ$  from  
839 figure 3.

840 Figure 8. Chondrite normalized REE patterns for zircons from four samples measured by SIMS  
841 (a. 1S82, b. 1S53, c. 1S79, d. 1S77) from the Dinkey Dome (1S82 and 1S79 from the west side,  
842 1S53 and 1S77 from the east side). Filled symbols are from cores and open symbols are rims.  
843 Background information for data presented in this figure can be found in supplementary data  
844 Table F.

845 Figure 9. (a)  $(\text{Sm}/\text{La})_N$  vs. La (ppm) in rims and cores of zircon in the Dinkey Dome, from the  
846 same four samples from figure 8 (1S82, 1S53, 1S79, 1S77). (b)  $\text{Ce}/\text{Ce}^*$  vs.  $(\text{Sm}/\text{La})_N$  in rims and  
847 cores from zircon in the Dinkey Dome, from the same four samples as in (a). Magmatic and  
848 hydrothermal fields from Hoskin (2005) and Grimes et al. (2007). Background information for  
849 data presented in this figure can be found in supplementary data Table E.

850 Figure 10. Evolution of  $\delta^{18}\text{O}$  of zircon and garnet in the Dinkey Dome pluton recording  
851 assimilation and fractional crystallization through time for the (a) western and (b) eastern sides  
852 of the pluton.

853 Figure 11. Model of the genesis of the Dinkey Dome pluton from the earliest stage (I)  
854 increments of melt transiting wallrocks of different  $\delta^{18}\text{O}$  in the presence of early stage zircon, to  
855 (IV) final stage crystallization of garnet in the composite pluton.

856

857

858

859

860

861 Table 1. Oxygen isotope data summary.

Sample	Lithology	$\delta^{18}\text{O}$ WR ‰ VSMOW (laser)	$\delta^{18}\text{O}$ Zrn ‰ VSMOW (laser)	$\delta^{18}\text{O}$ Zrn ‰ VSMOW (SIMS)	$\delta^{18}\text{O}$ Grt ‰ VSMOW (laser)	$\delta^{18}\text{O}$ Grt <sub>Ave</sub> ‰ VSMOW (SIMS)	$\Delta^{18}\text{O}$ (Grt <sub>Ave</sub> - ZrC <sub>Ave</sub> )
1S51	granite	9.71*	7.76*	C=7.6, R=7.3	6.9	6.2	-1.4
1S52	granite	9.80*	7.51*	C=7.8, R=6.7	7.4	5.9	-1.3
1S53	granite	9.57*	7.53*	C=7.9, R=6.4	6.9	5.9	-1.4
1S54	granite	9.90*	7.81*	C=8.0, R=6.8		6.4	-1.0
1S58	granite	9.90*	7.77*	C=7.5, R=7.0		7.4	0.1
1S77	granite	9.81*	7.63*	C=7.6, R=6.5	6.9	7.0	-0.4
1S79	granite	9.96*	7.67*	C=7.6, R=6.8	7.7	7.5	0.2
1S80	granite	10.30*	7.72*	C=8.1, R=6.3	7.9	7.3	0.1
1S81	granite	9.79*	7.76*	C=7.7, R=7.1	7.2	7.4	0.0
1S82	granite	9.79*	7.73*	C=7.8, R=7.3	8.0	7.6	-0.1
10DD-02	granite	10.47		7.9**		7.1	-0.8
10DD-05	granite	10.14		7.4**		6.7	-0.7
10DD-06	granite	9.65					
10DD-07	granite	9.41					
10DD-08	granite	9.48					
10DD-10	bt hornfel	12.72					
10DD-15	quartzite	11.82					
10DD-16	granite	9.35		7.6**		5.7	-1.9
10DD-17	granite	9.12		6.9**		5.1	-2.0
10DD-18	granite	8.96					
10DD-19	granite	9.06		7.0**		5.0	-2.0
10DD-20	enclave	8.25					
10DD-21	granite	9.17					
10DD-22	granite	9.06					

\*Lackey et al. (2006) oxygen isotope analyses by Laser Fluorination.

\*\*SIMS analyses on grains too small to distinguish core vs. rim.

C=Core, R=Rim; Zrn=Zircon, Grt=Garnet, WR=Whole Rock.

Samples 1S51 - 1S82 are grain mounts; 10DD-02 - 10DD-22 are thin sections.

862

863 **Supplementary Data Tables:**

864 Supplementary Table A: Sample locations and  $\delta^{18}\text{O}$  summary.

865 Supplementary Table B: EPMA data.

866 Supplementary Table C: Zircon SIMS  $\delta^{18}\text{O}$  data.

867 Supplementary Table D: Garnet SIMS  $\delta^{18}\text{O}$  data.

868 Supplementary Table E: Garnet Laser Fluorination  $\delta^{18}\text{O}$  data.

869 Supplementary Table F: Zircon REE data.

Fig. 1

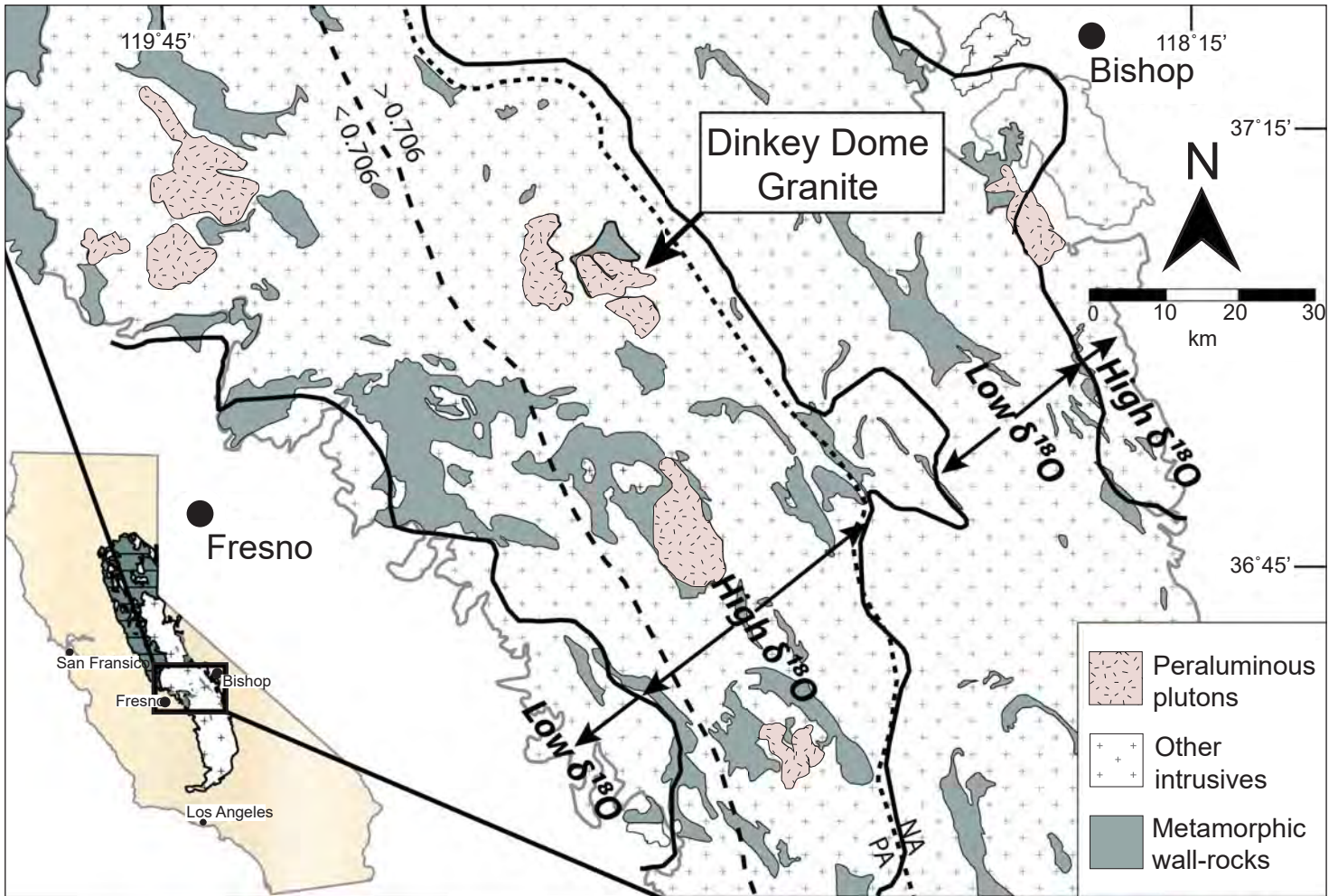




Fig. 2

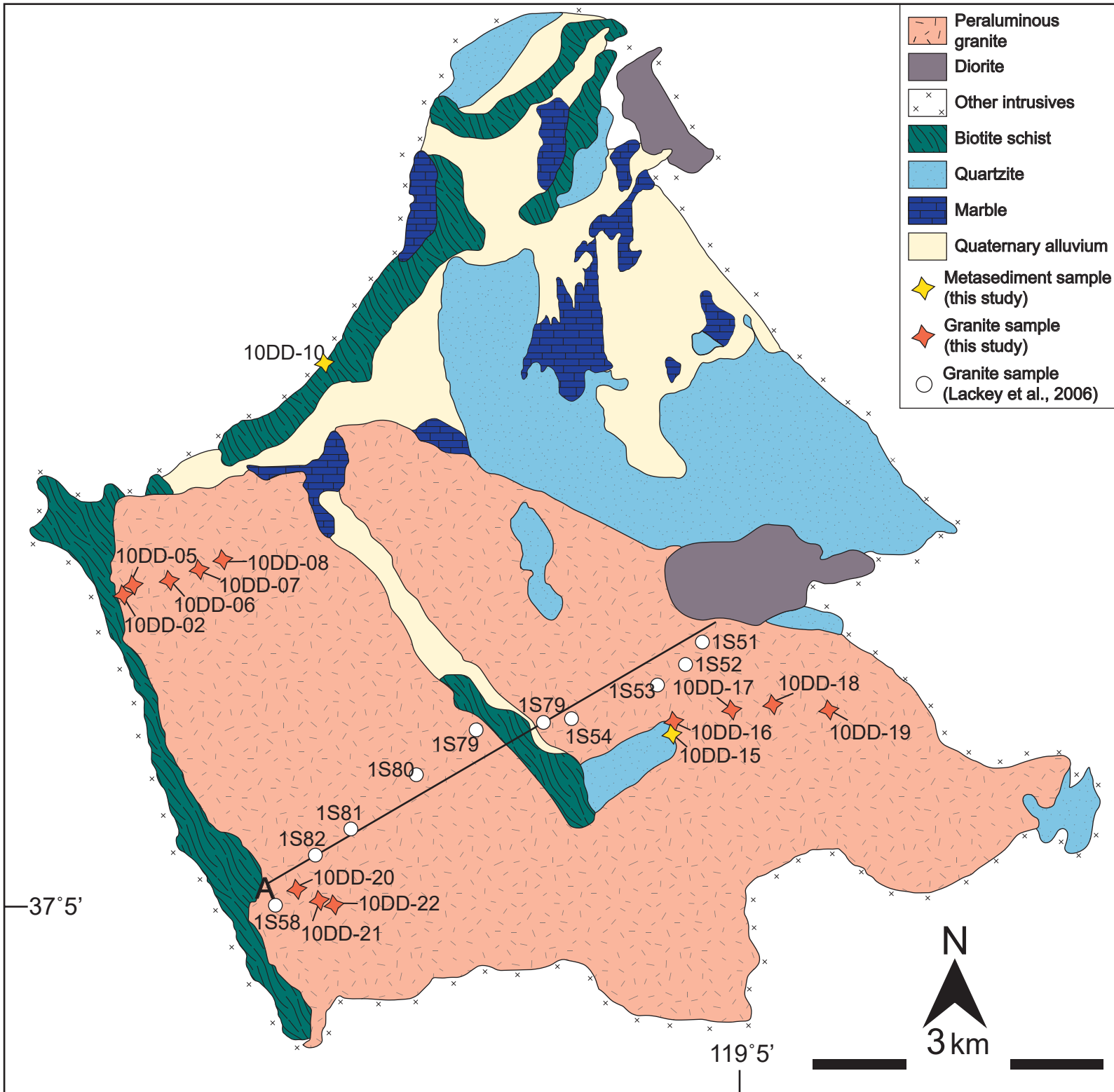


Fig. 3

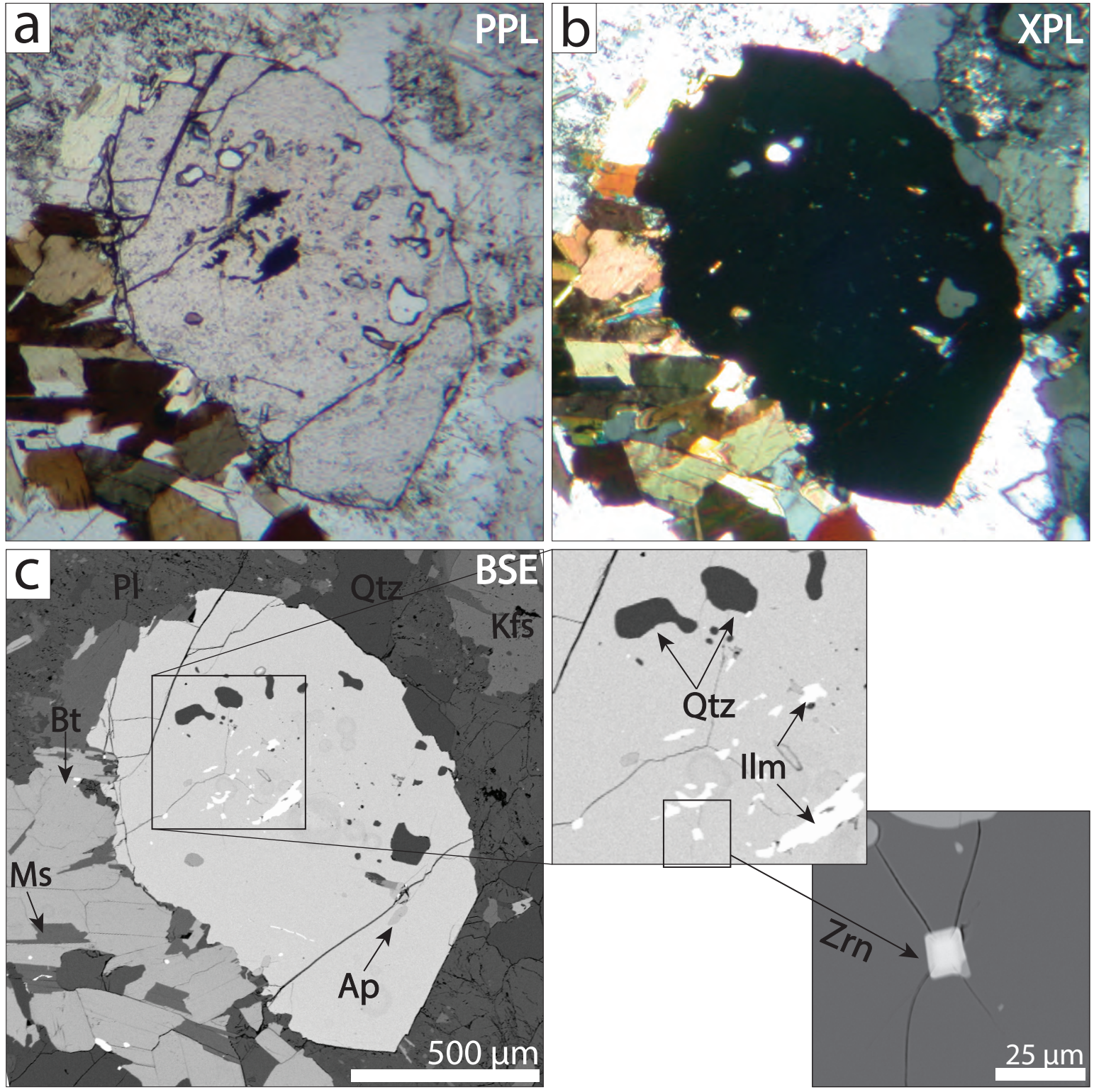


Fig. 4



Fig. 5

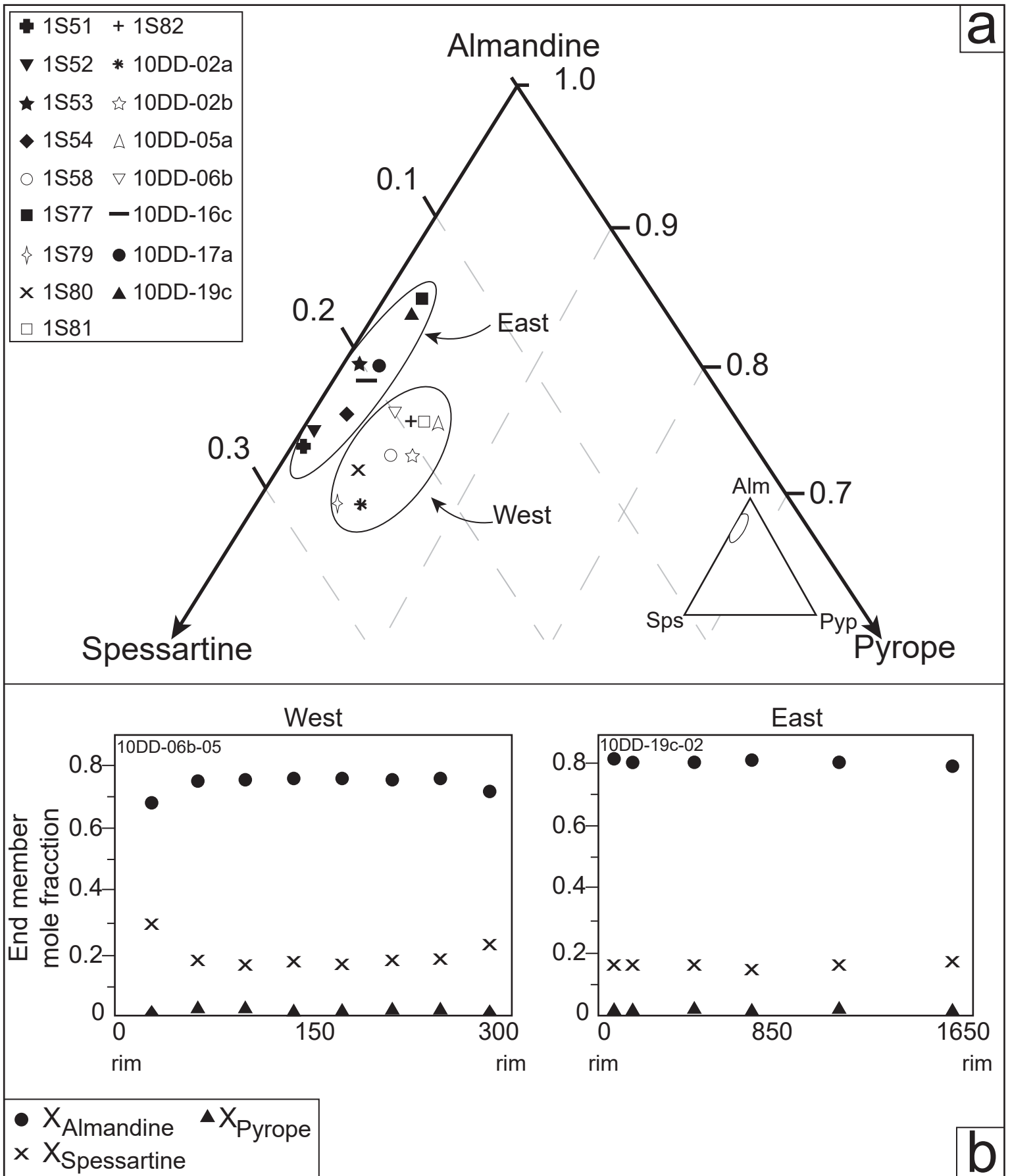


Fig. 6

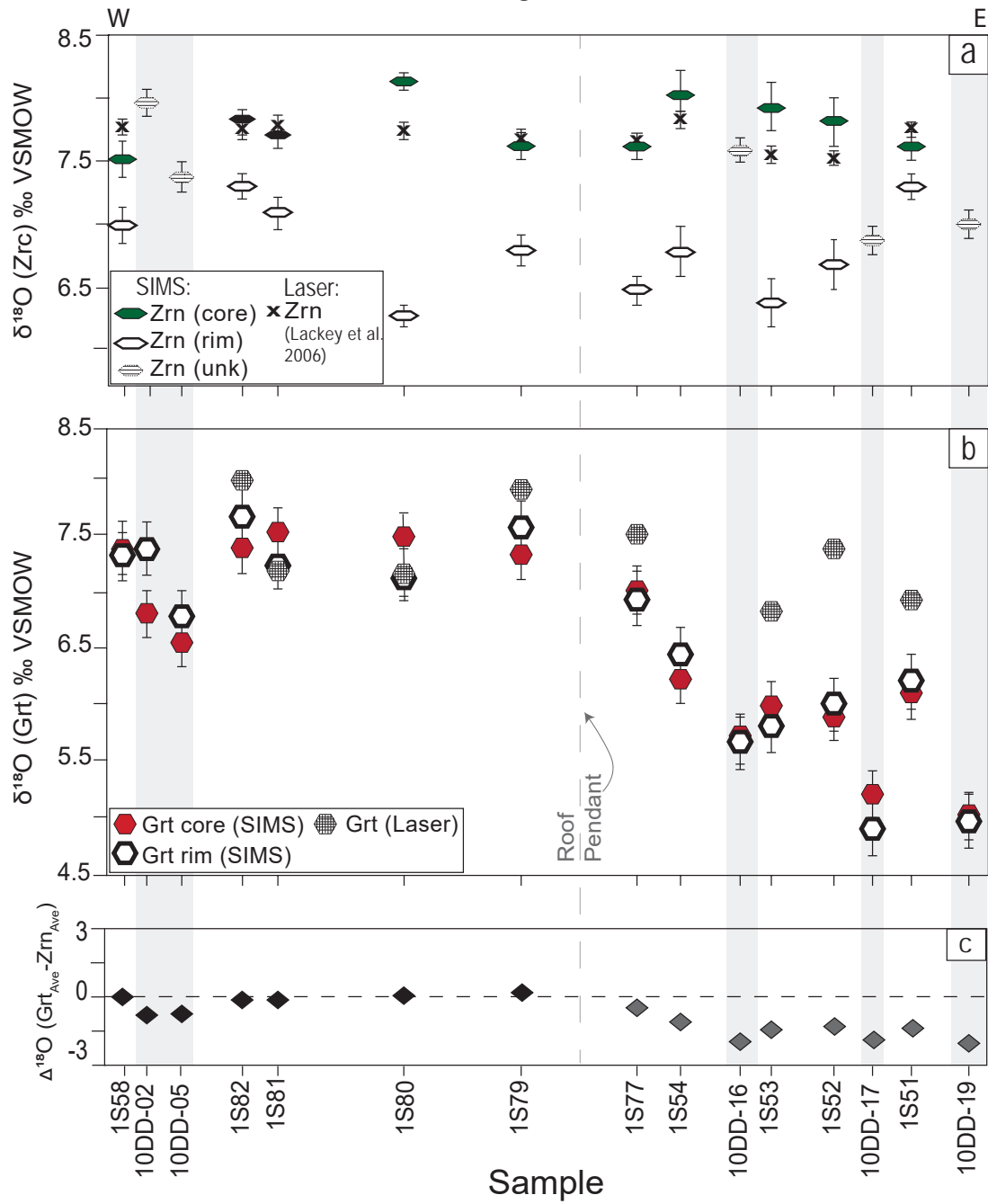


Fig. 7

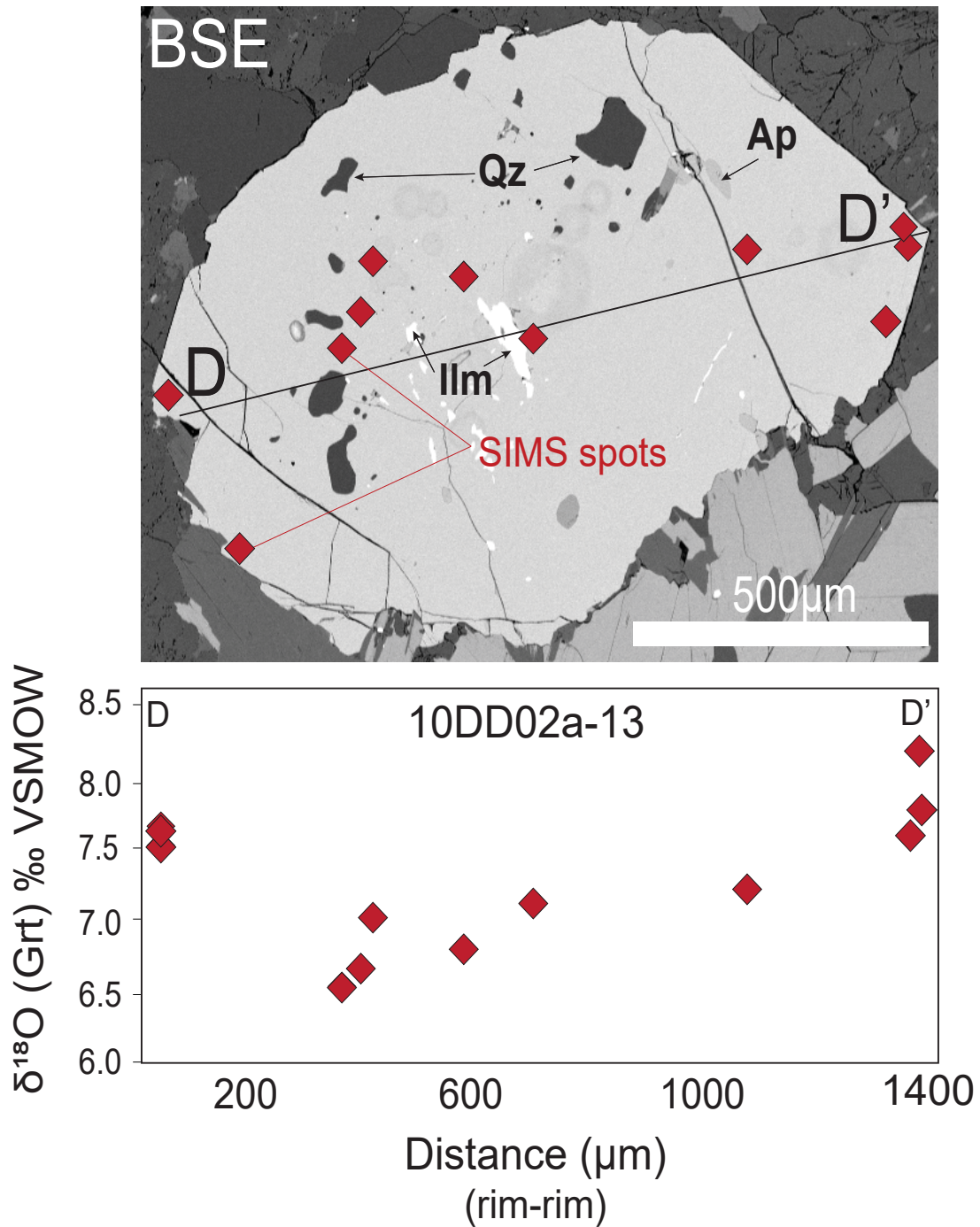


Fig. 8

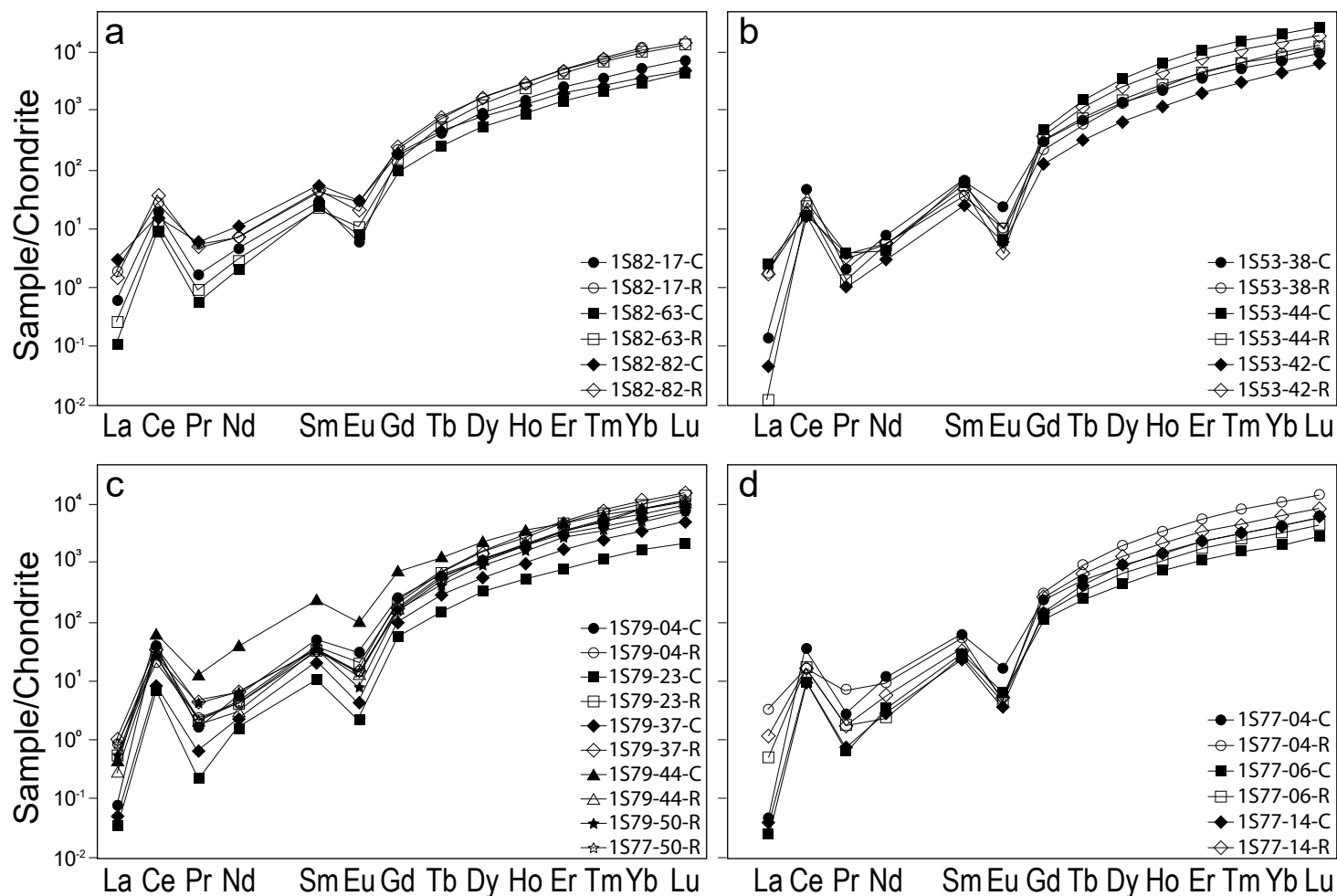


Fig. 9

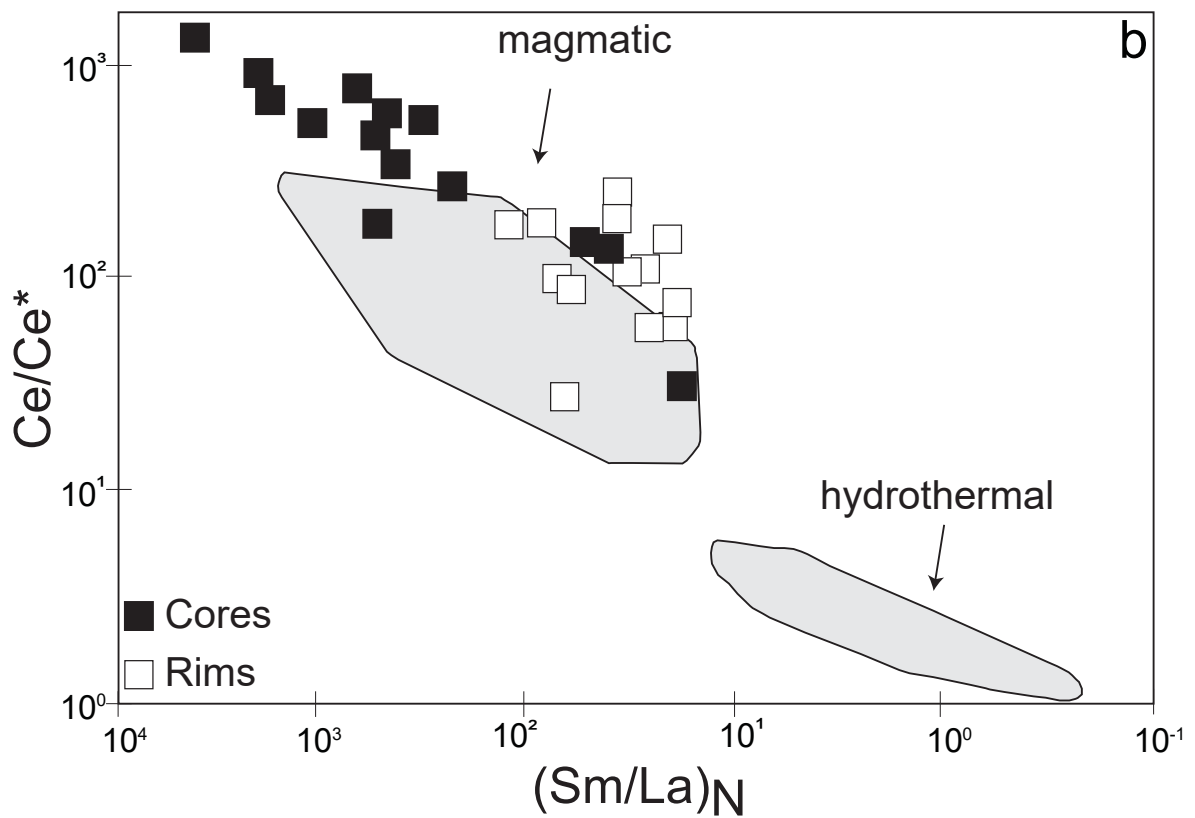
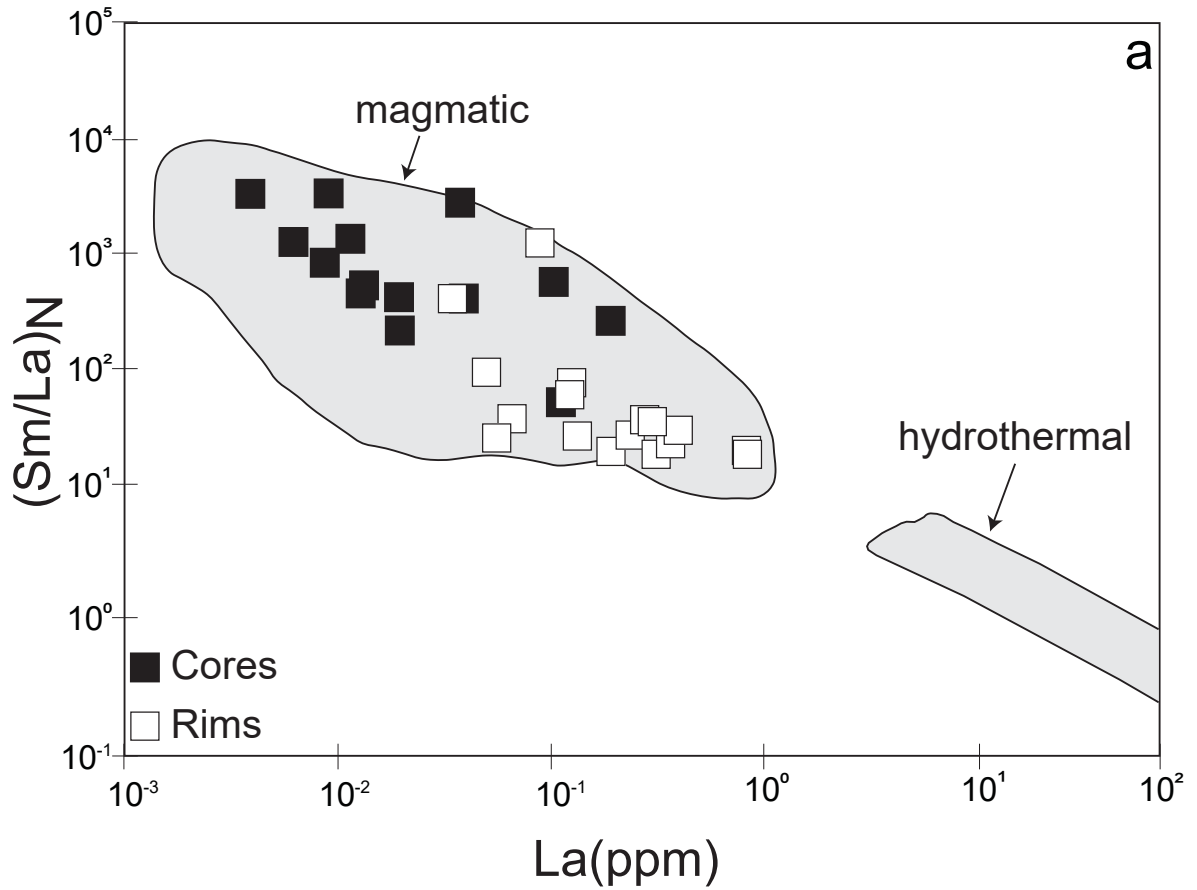




Fig. 10

